Comparing the reactivity of glasses with their crystalline equivalents: the case study of plagioclase feldspar

Anne Perez, Damien Daval, Maxime Fournier, Mélanie Vital, Jean-Marc Delaye, S. Gin

Comparing the reactivity of glasses with their crystalline equivalents: the case study of plagioclase feldspar

Anne Perez[1,2*], Damien Daval[1], Maxime Fournier[3], Mélanie Vital[4], Jean-Marc Delaye[3] Stéphane Gin[3]

[1] LHyGeS, CNRS, Université de Strasbourg, UMR 7517, 1 rue Blessig 67084 Strasbourg, France

[2] LGE, Université Paris-Est, Laboratoire Géomatériaux et Environnement, (EA 4508), UPEM, 77454 Marne-la-Vallée, France

[3] CEA, DEN, DE2D, SEVT, F - 30207 Bagnols sur Cèze, France

[4] Departamento de Química, Universidad Nacional de Mar del Plata, 722. Funes 3350, 7600 Mar del Plata, Argentina

* Corresponding author: anne.perez@u-pem.fr

Abstract

To evaluate the impact of atomic short- and long-range orders on silicate dissolution kinetics, the dissolution of amorphous and crystalline oligoclase was investigated at pH 1.5 and 10 at 90°C. Experiments in solution saturated with respect to $SiO_{2\ am}$ were additionally performed to constrain the effect of Si-rich surface layer formation on dissolution rates. The face-specific dissolution rates of the crystalline oligoclase and of the oligoclase glass were determined from element budget in solution and surface retreat measured by vertical scanning interferometry. The results show that atomic ordering primarily impacts solid reactivity, irrespective to the pH of the solution. A strong relation between the crystal surface orientation, the evolution of its topography and its dissolution rate was observed. The (001), (010) and (10-1) flat faces containing the strongest bonds dissolved the most slowly and their dissolution rates remained constant throughout the experiments. In contrast, the stepped (1-11) face was characterized by the highest initial dissolution rate, but progressively decreased, suggesting that the preferential dissolution of stepped sites expose afterwards more stable planes. The differences in terms of etch pit density from one surface to another also explained the difference in dissolution rates for the (001) and (010) faces. The fluid chemistry suggested the formation of very thin (100-200 nm) Si-rich surface layers in acidic conditions, which weakly affected the dissolution rate of the pristine crystal. At pH 1.5, oligoclase glass dissolves at a rate similar to that of the fastest studied faces of the crystal, suggesting the absence of structural effect on oligoclase dissolution. Whereas Si-rich surface layers likely formed by interfacial dissolution-reprecipitation for oligoclase crystal, molecular dynamic calculations suggest that the slightly more open structure of the glass could also allow ion-exchange following water diffusion into the solid. This mechanism could explain why the surface layer of the glass is characterized by a different chemical composition. Results at pH 10 are strikingly different, as the oligoclase glass dissolves up to 50 times faster than its crystalline equivalent. This non-linear response of

43 the material upon pH was linked to the density of critical bonds in oligoclase that is indeed
44 pH-dependent. In acidic pH, the preferential dissolution of Al leaves a highly polymerized
45 and relaxed Si-rich surface, whereas in basic pH the preferential dissolution of Si leads to a
46 complete de-structuration of the network because of the lack of Si-O-Al bonds.

1. Introduction

Predicting the reactivity of silicates over geological timescales is a fundamental concern in the environmental and Earth science fields. Modeling the long-term chemical weathering of silicate glasses is a particularly challenging issue. Glass alteration studies are essential to assess the environmental impact and insure the safe storage of highly radioactive wastes over the next hundreds of thousands of years (Grambow, 2006; Verney-Carron et al., 2008; Libourel et al., 2011; Vienna et al., 2013; Geisler et al., 2015; Icenhower and Steefel, 2015; Gin et al., 2016). Investigating the dissolution mechanisms and kinetics of silicates is also crucial for geochemical concerns. As an example, the weathering of basaltic glass and silicate rock is extensively studied in the field and in the laboratory to properly assess the chemical mass balance of the oceans and evaluate the potential CO_2 sequestration by silicates (Galeczka et al., 2014; Johnson et al., 2014; Sissmann et al., 2014; Parruzot et al., 2015; Ducasse et al., 2018).

Numerous experimental studies introducing standardized short-term dissolution tests of silicate glass/minerals dissolution are described in the literature (Wolff-Boenisch et al., 2004; Golubev and Pokrovsky, 2006; Hellmann and Tisserand, 2006; Pierce et al., 2008; Arvidson and Lüttge, 2010; Daval et al., 2010; Hellmann et al., 2010; Fenter et al., 2014; Perez et al., 2015). The results of these tests, involving a wide variety of experimental conditions (such as pH, temperature, saturation index, electrolyte background, static/flow rate conditions) are used to provide empirical rate laws that can be implemented into geochemical models in order to estimate the long-term scale of the dissolution processes. However, this long-term reactivity of silicates cannot currently be properly predicted: the systematically observed kinetic laboratory/field discrepancy might be related to the underestimation of the impact of intrinsic properties of the dissolving silicate, poorly constrained compared to the impact of extrinsic parameters such as pH or the saturation state of the fluid (White and

Brantley, 2003). The progressive evolution of the surface area during the dissolution process and the impact of these physicochemical changes on dissolution rates should be taken into account to develop more realistic dissolution models (Lüttge et al., 2013). Recent studies showing that the structural anisotropy of a mineral induces changes in terms of surface area and reactivity during the dissolution process are nice illustrations of this assertion (Bandstra and Brantley, 2008; Daval et al., 2013; Godinho et al., 2014a, Gruber et al., 2014; Pollet-Villard et al., 2016a, b). The demonstration of the impact of various energy surface sites (dislocations, kink and step sites for minerals, differently coordinated Si surface groups for glasses) on dissolution rates is also a good example (Dove et al., 2008; Fischer et al., 2014; Pollet-Villard et al., 2016; Godinho et al., 2014a). Finally, the potential passivating role of amorphous silica-rich surface layers (ASSLs) developed during the weathering process has been shown as crucial for both crystalline and amorphous silicate structures (Casey, 2008; Gin et al., 2015; Hellmann et al., 2015; Gin et al., 2018). The formation of a gel layer on glass samples is most frequently attributed to an ion exchange between alkali and water diffusing through the surface, followed by a self-reorganization of the interdiffusion layer (Cailleteau et al., 2008; Frugier et al., 2008). However, a new mechanism initially built up for silicate minerals, suggesting that crystal surfaces dissolve congruently within a thin interfacial film of water and that an alteration layer forms by precipitation in this water film, has recently been put forward for glasses (Hellmann et al., 2012; Hellmann et al., 2015). Elucidating these mechanisms is currently a priority for both the mineralogical and material science communities, as different formation mechanisms of surface layers should imply distinct physicochemical properties of these layers and different impacts on the long-term dissolution kinetics of silicate materials (Grambow and Müller, 2001; Rébiscoul et al., 2004; Gin et al., 2015; Ruiz-Agudo et al., 2016).

In this context, this work has been undertaken as an attempt to compare the dissolution behavior of both crystalline and amorphous phases and improve the understanding of the impact of the intrinsic structure of a solid on its dissolution. To reach this goal, batch feldspar dissolution experiments were conducted at 90°C, in contact with ultrapure water solutions at very acid or very basic pHs. Such pHs were chosen on the basis of previous studies, in order to favor, or not, the development of surface layers. The oligoclase feldspar and a synthetic amorphous equivalent were submitted to identical experiments in order to highlight the effect of structural order/disorder on the dissolution process. Moreover, for the crystal, 4 crystalline orientations of oligoclase were studied, in order to highlight the impact of structural atomic bonding on the dissolution rates.

2. Material and Methods

2.1 Materials

Centimeter-sized oligoclase crystals were purchased from Mawingu Gems. The chemical composition of the samples ($Na_{0.83}K_{0.02}Ca_{0.07}Al_{1.06}Si_{2.96}O_8$) was determined by ICP-MS analysis after performing an alkali-fusion protocol.

The glass was prepared from the crystalline material. 10 g of crystal were placed in a platinum crucible. Glass preparation took place in a high-temperature furnace Carbolite HTF 1700 (Figure 1d). The temperature was increased up to 1500 °C and kept constant for 2 hours to homogenize the melt, then increased again up to 1650 °C to reduce its viscosity. After 2 hours at 1650 °C, the bottom of the crucible was poured into water to quench the silicate melt into a glass. The glass was finally annealed overnight at 550°C.

The structure of the two materials was analyzed by solid-state nuclear magnetic resonance spectroscopy (NMR) and X-ray diffraction (XRD). Results are displayed in Supplementary

Data. Briefly, these analyses showed that the glass is amorphous and contains negligible amounts of remaining oligoclase crystallites (< ~ 0.6 wt. %), as revealed by semi-quantitative processing of XRD patterns acquired on mixture of the glass samples with an internal standard of LaB6. In addition, the Si-Al crystal structure is highly ordered (Yang et al., 1986).

2.2 Sample preparation

Oligoclase samples were oriented along the (001), (010) and $(10\bar{1})$ preferential cleavages or cut following the $(1\bar{1}1)$ orientation (Figure 1a). The selection of the four oriented surfaces was made on the basis of the Periodic Bond Chain (PBC) theory (Hartman and Perdok, 1955). The PBC theory states that crystal faces can be sorted out according to the number of uninterrupted chains of energetically strong bonds (PBC) they contain. Faces containing respectively 2, 1 and no PBC are named F- (for flat), S- (for stepped) and K- (for kinked) faces. The structure of feldspars was studied by Woensdregt (1982) according to the PBC theory, who suggested to subdivide the F category between F1 and F2 subcategories, which contain only the strongest PBCs of the structure (only Al–O or Si–O bonds) or also contain weaker K–O or Na–O PBC, respectively. According to Woensdregt (1982), the (001) and (010) planes both belong to the F1 category, $(10\bar{1})$ belongs to the F2 category and $(1\bar{1}1)$ belongs to the S category. Oriented samples were then embedded in epoxy resin such that only the crystallographic face of interest was exposed at the epoxy surface, and polished through a multi-step abrasive sequence (Figure 1b). The crystallographic orientations were checked using Electron Backscatter Diffraction (EBSD) on a Tescan Vega 2 scanning electron microscope (SEM) (Figure 1c). The oriented samples were divided into small pieces and portions of their surfaces were protected with ~ 1 mm-diameter room-temperature-vulcanizing (RTV) glue spots.

147 The piece of oligoclase glass was cut into several pieces. These pieces were embedded
148 in epoxy resin, polished through a multi-step sequence with an ultimate polishing step in a
149 colloidal suspension (Figure 1e) and masked with glue spots (Figure 1f). The geometric
150 surface of each embedded sample was estimated after measurements carried out on binocular
151 photographs of the samples.

152 The initial roughness of each sample surface was measured with a vertical scanning
153 interferometer (VSI, ZYGO NewView 7300). For all samples, the initial average arithmetic
154 roughness (R_a), defined as the arithmetic average of the absolute values of the roughness
155 profile, ranged between 10 nm and 40 nm, and were measured on 180 × 180 µm² VSI images,
156 corresponding to the field of view imaged at the maximum magnification. The geometric
157 surface of each sample was calculated from the dimensions of the monoliths and ignoring the
158 surface roughness.

159

160 **2.3 Dissolution experiments**

161 Oligoclase samples were introduced into 120 mL PFA Savillex® reactors
162 continuously stirred with magnetic bars placed over PTFE tripods. The reactors were filled
163 with 80 mL of solution and incubated at 90°C.

164 Each studied sample was immersed either in pH 1.5 or pH 10 solutions (the given pH
165 values corresponds to the pH of the solution at 90°C), whose saturation indices with respect to
166 amorphous silica ($SiO_{2\ am}$) were equal to 0 or ~1. These solutions were prepared from
167 ultrapure water (18.2 MΩ·cm). High-grade HCl (37%, ACS reagent) and LiOH (Prolabo)
168 were used to adjust the pH. The solutions saturated with respect to $SiO_{2\ am}$ at 90 °C were
169 prepared by dissolving 0.36 g and 5.11 g of $SiO_{2\ am}$ (Merck Silicagel 60) in 1L of ultrapure
170 water for experiments conducted at pH 1.5 and 10, respectively.

171

172

2.4 Analyses

Our experimental strategy enabled us to obtain face-resolved fluid data with Inductively Coupled Plasma Atomic Emission Spectroscopy (ICP-AES) and to deduce the face-specific dissolution rate at the boundary between the surface layer and non-altered solid, which is referred below to as the "internal interface" (see Wild et al. (2016) for details). Conversely, the opposite boundary of the surface layer, located at the interface with the bulk solution is referred hereafter to as the "external interface". Our study benefited from the use of VSI to determine dissolution rates at this external interface.

2.4.1 Solution analyses by ICP-AES

Experiment durations ranged between 28 and 46 days, depending on the experimental conditions (pH, monoliths/powders, crystal/glass). Solution sampling was regularly carried out for the analyses of Si, Al and Na using ICP-AES (Thermo ICAP 6000). pH was also checked at each sampling time and adjusted by small additions of LiOH or HCl if necessary.

For each element *i*, the normalized mass loss NL_i (mg/m^2) from the mineral/glass into the solution was calculated at each sampling time using the following Eq. (1):

$$NL_i = \frac{[i]}{S/V \times x_i} \quad (1)$$

where $[i]$ is the concentration (mg/m^3) of the element *i* in solution, *S* the surface area of the material in contact with the fluid (m^2), *V* the volume of solution (m^3) and x_i the mass percentage of the element *i* in the solid. The variations of *V* due to sampling and evaporation were measured by weighing the reactors before and after sampling and taken into account in the calculation, whereas *S* was considered as the initial geometric surface area of the sample.

The equivalent thickness (or leaching depth) of the altered mineral/glass Eth_i (nm) was then calculated based on each elemental release following Eq. (2):

198 $$Eth_i = \frac{NL_i}{\rho} \quad (2)$$

199 where ρ is the density of the mineral (2.62 g/cm^3) or the glass (2.34 g/cm^3).

200 A summary of the experimental parameters used in all experiments is given in Table 1.

201 The theoretical thickness of amorphous Si-rich surface layers (ASSLs) developed on
202 each mineral surface was estimated on the basis of Na concentrations. A congruent reaction is
203 characterized by a stoichiometric release of Si, which is theoretically 2.96 times greater than
204 that of the measured Na concentrations. As a consequence, the difference between the
205 theoretical and measured Si concentrations, when negative, was attributed to the incorporation
206 of Si into a $SiO_{2\ am}$ surface layer, whose thickness e_{ASSL} (nm) was estimated at the end of each
207 experiment according to Eq. (3):

208 $$e_{ASSL} = \frac{\frac{\Delta m_{SiO_2}}{\rho_{SiO_2}}}{S_{geo}} \times 10^7 \quad (3)$$

209 where Δm_{Si} stands for the difference between the theoretical and measured mass of dissolved
210 SiO_2 in solution (g), ρ_{SiO_2} is the density of ASSL approximated to that of $SiO_{2\ am}$ (2.2 g/cm^3)
211 and S_{geo} is the geometric surface area (cm^2) of the sample exposed to the fluid.

212

213 *2.4.2 Surface topography measurements with VSI*

214 At each sampling time, the sample was removed from the solution. The RTV mask
215 was pulled off and the sample topography was measured with VSI in stitching mode
216 (magnification: ×5) to evaluate average changes in height between the unreacted reference
217 surface and the reacted mineral surface (Figure 2). Surface imaging was also performed at
218 higher magnification (×100) in order to follow the nucleation of etch pits. The data were
219 analyzed with the Metropro software.

220 After each VSI analysis, a new RTV glue spot was cautiously placed on the non-
221 dissolved area of the surface. After 24 hours (required for the glue to be completely dried), the

sample was rinsed in ultrapure water and re-immersed for five more days. This procedure was repeated until the experiment was completed. It was previously shown that the drying-wetting cycles to which the samples were submitted following this protocol do not impact the dissolution rate of the dissolving phase (Pollet-Villard et al., 2016a). As shown below, the observed linear increase of the mean surface retreat with time for most samples supports this assertion for oligoclase dissolution.

2.4.3 Calculation of dissolution rates

Equivalent thickness calculations and surface retreat measurements allowed for the determination of dissolution rates at the internal (R_{int}) and external (R_{ext}) interfaces (mol/m^2/s) following Eq. (4) (e.g., Smith et al., 2013). Because the release of Si and Al in the fluid is the result of several processes such as the formation/dissolution of the ASSL concomitantly to the dissolution of the pristine mineral, Na was chosen as a tracer specific to the dissolution at the internal interface.

$$\begin{cases} R_{int} = \frac{\Delta Eth(\mathrm{Na})}{\Delta t} \times \frac{1}{V_m} \\ R_{ext} = \frac{\Delta h}{\Delta t} \times \frac{1}{V_m} \end{cases} \quad (4)$$

where ΔEth(Na) is the variation of equivalent thickness (m) based on Na release in solution, Δh is the average height difference (m) between the reacted and the non-reacted surface, Δt is the experiment time (s) and V_m is the molar volume of oligoclase mineral/glass, which is equal to 1.0×10^{-4} and 1.1×10^{-4} m^3/mol, respectively.

Uncertainties on cation concentrations were considered as 10% of the analytical data values and are represented on the corresponding plots as error bars.

246 **2.5 Molecular dynamics calculations**

247 To better understand the discrepancies between the glass and crystal reactivities (i.e.,
248 dependence of the dissolution rate on pH and on the formation of ASSLs), molecular
249 dynamics (MD) calculations were performed, aimed at providing quantitative constraints on
250 the structure of the two solids.

251

252 *2.5.1. Computational details*

253 Classical molecular dynamics force fields as detailed in Deng and Du (2016) were
254 used to simulate vitreous and crystalline albite (whose composition is close to the oligoclase
255 used in the present study: 74.4 mol% SiO_2 – 12.7 mol% Na_2O – 12.9 mol% Al_2O_3) systems.
256 Buckingham type potentials were used:

257 $$\Phi(r_{ij}) = \frac{q_i q_j}{r_{ij}} + A_{ij} exp\left(-\frac{r_{ij}}{\rho_{ij}}\right) - \frac{C_{ij}}{r_{ij}^6} \quad (5)$$

258 where r_{ij} refers to the distance between the atoms i and j, and q_i and q_j refer to their atomic
259 charge. The adjustable parameters (A_{ij}, ρ_{ij} and C_{ij}) are given in Table 2. The charges are
260 respectively equal to 1.89, 1.4175, 0.4725 and –0.945 for the Si, Al, Na and O species.

261 The Coulombic interactions were treated with the complete Ewald summation with a
262 precision of 10^{-5} and the cutoff radius for the pair terms was equal to 10Å.

263 A simulation box containing 10,000 atoms has been prepared. It has been shown
264 recently that 10,000 atoms are largely sufficient to represent the short and medium – range
265 orders in silicate glasses (Deng and Du, 2018; Tilocca, 2013). The glass was prepared using
266 the following method: A liquid was first equilibrated at 4,000K during 100,000 time steps.
267 After this, a first quench was applied at 1.10^{12} K/s until 3,000K in the NVT ensemble
268 (constant number of atoms (N), constant volume (V) and constant temperature (T)).
269 Practically, a stepwise decrease of the temperature was applied in several 20,000 time step
270 stages with a temperature difference (ΔT) equal to 20K between two successive stages. A

second quench was applied at 10^{11}K/s between 3,000K and 300K. For this second quench, each stage lasted 200,000 time steps and the ΔT was equal to 20K. A 100,000 time step final equilibration was applied at 300K in the NVE ensemble (constant number of atoms (N), constant volume (V) and constant energy (E)) to accumulate 21 intermediate configurations (separated each by 5,000 time steps). The structural analysis described in this article corresponds to averages performed on these 21 configurations. The time step was equal to 1 fs for all stages of the glass preparation. A density of 2.38 g/cm^3 was imposed during the glass preparation, and the pressure was fixed at 1 atm.

Using the same interatomic potentials, the structure of crystalline albite was also simulated. The crystalline structure was considered as initial configuration and a 10,000-time step relaxation was applied to release the local stresses.

2.5.2. Interstitial site distributions

As in Malavasi et al. (2006), Kerrache et al. (2014) and Mansas et al. (2017), the interstitial site distributions were calculated for the glass and crystalline systems. The interstitial site distributions were calculated using a code provided by Pedone et al., 2006. This code identifies all the Delaunay tetrahedra present in a structure and calculates the free volumes inside each of them. Briefly, Delaunay's tessellation consists in paving the total space by tetraedra formed by four adjacent atoms. An interstitial site is associated to each Delaunay tetrahedron. The volume of an interstitial site, V_{free}, is determined by subtracting the volume occupied by the four atoms to the volume of the tetrahedron. Then, V_{free} is converted into an equivalent radius r_{eq}:

$$V_{free} = \frac{4}{3}\pi r_{eq}^3 \quad (7)$$

The atomic radii considered were equal to 0.41 Å, 1.10 Å, 0.50 Å, and 0.95 Å for Si, O, Al, and Na atoms respectively. The Si radius corresponds to the values proposed by Shannon et

al. (1969) or Pauling (1947). The O radius corresponds to half the distance between O atoms in O_2 molecule. This value was chosen to guarantee that the sum of the radii of two neighboring atoms remains lower than the distance between them. For the same reason, the Al radius was slightly reduced to 0.50 Å (instead of 0.53Å for the Pauling radius) to guarantee that each Al-O distance remains larger than the sum of their radii.

3. Results

The elemental concentrations measured in the reactors along all dissolution experiments are reported in Table 3.

The CHESS code (van der Lee and De Windt, 2002) was used to determine the saturation indices with respect to oligoclase and secondary phases. The thermodynamic database used was Chess (http://chess.ensmp.fr), which is derived from the Lawrence Livermore National Laboratories EQ3/6 database (version 8; release 6). All solutions at pH 1.5 (Si-rich and low concentration) and at pH 10 (Si-low concentration) were undersaturated with respect to oligoclase and secondary products. Experiments at pH 10 in Si-rich solutions were given saturated with respect to petalite and spodumene, which are two Li-rich aluminosilicates. Such minerals were not observed in our systems, as they are unlikely to be formed via an aqueous synthesis at low temperature (as an example, Li et al. (2013) showed that temperature as high as 570 °C was required for the crystallization of spodumene from aqueous solutions).

Surface retreat measurements and normalized mass losses (Si, Al, Na) are depicted in Figures 3 to 10 for all crystalline and amorphous samples, and the associated dissolution rates are listed in Tables 4 and 5.

Because of the multiplicity of experimental parameters investigated in this study, the results are organized below considering the pH of the solutions as the primary parameter, and the saturation index with respect to amorphous SiO_2 as the secondary parameter. The results regarding the glass sample are systematically described in comparison to those obtained on the four oriented surfaces of the crystal.

3.1. Oligoclase dissolution at pH 1.5

3.1.1. Experiments conducted in Si-low solutions

The temporal evolution of surface retreat and corresponding altered thickness are depicted in Figure 3 for Si-low experiments conducted at pH 1.5 on the four oriented surfaces of the oligoclase crystal. Overall, the dissolution rates reported in Table 4 bracket the dissolution rates that can be calculated based on the oligoclase dissolution rate parameters provided by Palandri and Kharaka (2004) at acidic pH conditions (4.8×10^{-9} mol/m²/s).

The retreat of the selected flat (F1, F2) faces appears to increase linearly with time. In contrast, the $(1\bar{1}1)$ stepped (S) face exhibits a non-linear surface retreat with time. From day 0 to 20, the dissolution of the stepped face at the external interface is characterized by the highest dissolution rate among all the studied faces. However, after 10 days, the reactivity of the surface gradually decreases down to a dissolution rate equivalent to those calculated for the slower flat faces ($<1.0\times10^{-8}$ mol/m^2/s, see Table 4). Surface retreat data also show the surprisingly high reactivity of the (001) F1 face, expected to be one of the slowest dissolving face according to the PBC theory. The (001) surface appears to dissolve 3 times faster than the other selected F1 face (Table 4), at a rate equivalent to the one calculated for the $(10\bar{1})$ F2 face.

These discrepancies are also evidenced in the fluid data (*Eth* data plotted in Figure 3 and dissolution rates at the internal interface given in Table 5), which are characterized by the same trends.

The dissolution of the 4 faces appears to be congruent within uncertainties: the normalized concentrations are virtually superimposed for all datasets (Figure 3).

These results obtained for the crystal can be compared to those obtained by dissolving the glass in identical experimental conditions (Si-low solution at pH 1.5 and 90°C; Figure 4). Here again, the surface retreat and *Eth* values increase linearly with time. Both VSI and fluid data suggest that the glass dissolves at a rate intermediate to that of the fastest and slowest flat faces of the crystal (see Tables 4 and 5). The glass dissolution is incongruent: the $\frac{Na}{Si}$ and $\frac{Al}{Si}$ ratios in solution are ~ 1.5 times higher than the ratios calculated according to the composition of the glass. Finally, a systematic difference between the *Eth* and Δh values is evidenced for each crystallographic orientation, as well as for the glass sample. This observation is further discussed in section 4.1.

3.1.2. Experiments conducted in solutions saturated with respect to $SiO_{2\ am}$

In the experiments conducted on crystalline samples at pH 1.5 in solutions saturated with respect to $SiO_{2\ am}$, the surface retreat is below the vertical detection limit of VSI (~ 3 nm). Moreover, in such solutions characterized by high concentrations of Si, slight variations in Si concentrations resulting from oligoclase dissolution could not be properly quantified. As a consequence, only the evolution of the normalized concentrations of Al and Na with time is plotted in Figure 5, for the four selected orientations of the crystal.

The *Eth* values globally follow a linear trend with time, for all the selected faces. The trends might be slightly curved in these experimental conditions compare to experiments carried out in Si-low systems. The release of Na and Al is congruent, within uncertainties, and

the calculated dissolution rates at the internal interface range between 4.0×10^{-9} and 9.0×10^{-9} mol/m^2/s (Table 5). As observed in Si-low solutions, the (010) face is characterized by the slowest dissolution rate (Table 5).

These face-specific results can be compared to those obtained for the glass in the same experimental conditions and are depicted in Figure 6.

The reported surface retreat data enable the calculation of a dissolution rate at the external interface of the glass sample in saturated conditions. External and internal dissolution rates are ~ 4 times lower than those determined for the glass in Si-low solution (Figure 6, Table 5). The glass dissolution is incongruent: as observed in Si-low experiments, Na is released 1.5 times faster than Al.

3.2. Oligoclase dissolution at pH 10

3.2.1. Experiments conducted in Si-low solutions

The temporal evolution of the surface retreat and normalized Si, Na and Al concentrations in the fluid are shown in Figure 7 for the 4 selected faces of the crystal at pH 10 and 90°C. In a general manner, surface retreats and *Eth* values follow the trends depicted at pH 1.5 (Figures 3). The data suggest that the internal and external dissolution rates of the (001), (010), $(10\bar{1})$ flat surfaces are constant, whereas the dissolution of the $(1\bar{1}1)$ stepped surface is characterized by a decrease in both external and internal dissolution rates with time. The (001) F1 surface dissolves at external and internal rates equivalent to those calculated for the $(10\bar{1})$ F2 face (~ 1.0×10^{-9} mol/m^2/s and ~ 8.0×10^{-9}, respectively), whereas the (010) F1 face is the slowest dissolving face, with dissolution rates at the external and internal interfaces 3 times lower than those obtained for the (001) F1 face.

The oligoclase crystal dissolves more slowly at pH 10 than at pH 1.5. The calculated dissolution rates at the external and internal interfaces are almost 10 times lower than those

395 determined at pH 1.5 (Tables 4 & 5). Moreover, the $\frac{Na}{Si}$ ratio in solution is stoichiometric. In
396 this case, no Si-rich surface layer is suspected to form.
397 These results obtained for the crystal can be compared to those obtained by dissolving
398 the glass in identical experimental conditions (Si-low solution at pH 10 and 90°C). They
399 reveal a drastic change (Figure 8). According to both surface retreat and *Eth* values, the glass
400 dissolution rate is 10 to 20 times (depending on the considered oriented surface) greater than
401 its crystalline equivalent.
402 The surface retreat data and *Eth* values follow a linear evolution with time. The
403 dissolution of the glass is congruent throughout the experiment.
404 As a final observation, systematic differences between the *Eth* and Δ*h* values are
405 evidenced for each crystallographic orientation, as well as for the glass sample, similarly to
406 the results obtained at pH 1.5 in Si-low solutions. This observation is further discussed in
407 section 4.1.
408
409 *3.2.2. Experiments conducted in solutions saturated with respect to $SiO_{2\ am}$*
410 As observed for experiments carried out at pH 1.5, no surface retreat was detected on
411 samples dissolved at pH 10 in solutions saturated with respect to $SiO_{2\ am}$. As a consequence,
412 only the evolution of the normalized concentrations of Al and Na with time in such Si-rich
413 solutions is shown in Figure 9, for the four selected orientations of the crystal.
414 These results show that Al concentrations are below the detection limit of the ICP-
415 AES, in all experiments. Na is the only detected element. A progressive decrease in Na
416 release rates is observed with time. While the solution is undersaturated with respect to any
417 phases that may be prone to precipitate at high temperature, such as aluminum
418 (oxy)hydroxides or phyllosilicates, the collected aqueous samples are oversaturated with
419 respect to boehmite and pyrophillite at ambient temperature, if one supposes a congruent

release of Al and Na. As suggested in previous studies (e.g., Verlaguet and Brunet, 2007), the lack of Al may therefore be related to the quench phase of the experiment, when the temperature is decreased from 90 °C (where Al is soluble) to room temperature (where Al is no longer soluble).

As a comparison, dissolution measured at the internal and external interfaces are plotted in Figure 10 for the glass sample. The evolution of surface retreats and *Eth* values with time exhibit a curved shape. Here again, the glass appears to dissolve much faster than the crystalline oligoclase at both external and internal interfaces (from 10 to 20 times faster, depending on the considered crystallographic orientation, see Tables 4 & 5). In addition, the Al and Na cations are not released congruently.

4. Discussion

4.1. Apparent inconsistencies between VSI and fluid data

Strikingly, the dissolution rate calculated based on cation release is systematically greater than that calculated using VSI data, by a ~1.3 to ~7 fold-factor (see Figures 3, 4, 7, 8). Several explanations may account for this observation: first of all, the surface retreat was calculated based on VSI data purposely acquired in the direct vicinity of the mask (see Figure 2), which was roughly centered on the surface of the considered crystal face. As emphasized in previous studies (e.g., Saldi et al., 2017), such measurements miss the contribution of edge and corner dissolution, where the density of steps and kinks dramatically increases compared to the flat surface of a crystallographic plane (note that as reported in Robin et al. (2018), the difference of hardness between the sample and the epoxy resin results in crystals being slightly above the level of the resin after polishing, so that their edges and corners may still contribute to the dissolution). While edges and corners participate in the total flux of

dissolved matter, including their contribution in the present analysis is poorly relevant to discuss the dissolution anisotropy of oligoclase, as their respective contribution depends on the ratio of the total edge length to the flat surface area, which is not an intrinsic feature of oligoclase, but a specific aspect of the geometry and dimensions of the crystals selected to conduct the experiments. For this reason, the discussion of dissolution anisotropy detailed in the subsequent section 4.2 is based on the dissolution rates calculated from VSI data, rather than those calculated from the fluid data.

More generally, several studies emphasized that the dissolution rate of minerals is heterogeneous, and is dramatically impacted by defects and/or discontinuities such as polishing scratches, twinings and grain boundaries (e.g., Burch et al., 1993; Emmanuel and Levenson, 2015; Fischer et al., 2015; Fischer and Luttge, 2017). Beyond the mean surface retreat reported in the present study, specific hotspots of reactivity may be highlighted using the "rate spectra" concept (Fischer et al., 2012). An illustration of this assertion for the (010) face is reported in Figure 11a. Whereas the dissolution rate of the overall surface is reasonably well explained by a single mode in locations devoid of polishing scratches, their contribution to oligoclase dissolution is responsible for the appearance of a second mode with greater reactivity (Figure 11b). The consideration of the whole surface of the crystal (i.e., including polishing scratches) almost doubles the mean dissolution rate of the (010) face dissolved at pH 1.5, partly filling the gap between the fluid and VSI data. Finally, the progressive development of internal porosity such as microchannels and microtubules (e.g., Fisk et et al., 1998, Fisk et al., 2013), impossible to probe with surface-sensitive techniques, may also contribute to the difference between VSI-derived and ICP-AES-derived rate data.

Overall, the apparent inconsistencies between VSI and fluid data may be attributed to the dissolution of crystal edges and corners, as well as polishing scratches, which we

purposely ignored in the treatment of our data to better capture the intrinsic dissolution of a crystallographic plane in a considered direction. These results are discussed below.

4.2. Dissolution anisotropy

The results obtained for the crystal at both pHs strongly suggest that atomic ordering primarily impacts solid reactivity. First of all, the shape of the $\Delta h(t)$ and $Eth(t)$ relations varies depending on crystallographic orientation. The face-specific dissolution experiments are characterized by a linear increase of surface retreat/equivalent thickness with time for the (001), (010), $(10\bar{1})$ flat faces. In contrast, the dissolution of the $(1\bar{1}1)$ stepped face exhibits a parabolic trend.

On a crystal surface, steps are formed by the interception of two stable planes (Figure 12). The atoms located at the steps have a lower coordination number. As a consequence, they represent high energy sites on a mineral surface and are potentially more likely to be released in solution. As dissolution progresses, the density of steps should decrease, exposing larger areas of more stable planes, characterized by a lower surface energy. Such observations have been made in several studies on the dissolution of fluorite (Godinho et al., 2013; Godinho et al., 2014a; Godinho et al., 2014b; Maldonado et al., 2013) and calcite (Smith et al., 2013). This scenario is consistent with the obtained results for oligoclase crystal, which show an initially fast dissolution period characterized by the highest dissolution rate among all the studied faces (e.g., 1.5×10^{-9} mol/m^2/s at pH 10), followed by a dissolution at a rate equivalent to those calculated for the flat faces (7.3×10^{-10} mol/m^2/s at pH 10). This suggests that (i) the evolution of the surface topography of a stepped face may control its long-term dissolution rate and (ii) the most stable surfaces of oligoclase, which dissolve slower, tend to persist during the dissolution process.

493 Secondly, the differences in the face-specific dissolution rates can in part be explained
494 in terms of the crystallographic bonding structure. Our measurements verify that the face
495 reactivity is correlated with the strength of the bonds they contain, as expected from the PBC
496 theory. The (001) and (010) surfaces, containing the strongest bonds (Si-O and Al-O only),
497 are the less reactive surfaces among the selected faces of oligoclase. The low reactivity of the
498 (001) and/or (010) faces was previously evidenced by Zhang and Lüttge (2009) and Pollet-
499 Villard et al. (2016a). The $(10\bar{1})$ face, containing weaker bonds (Si-O, Al-O but also Na-O),
500 appears to dissolve faster than the two F1 faces. Finally, during the first stages of experiments
501 (about 10-20 days), the stepped face is the fastest dissolving face.
502 If one admits that, as predicted by the PBC theory, the initial reactivity of the selected
503 faces decreases following the order S > F2 > F1, then the (001) F1 face dissolves
504 anomalously faster than the (010) F1 face. This divergence between the reactivity of the
505 (001) and (010) faces is also reflected by the microstructure of the different surfaces
506 revealed at pH 10: The (001) flat surface is characterized by a high density of etch pits,
507 contrasting with the (010) flat surface, on which the pit density is much lower (Figure 13).
508 Mineral dissolution has been shown to be strongly linked to the formation of etch pits
509 (Pollet-Villard et al., 2016a; Pollet-Villard et al., 2016b; Arvidson *et al.*, 2003; Beig and
510 Luttge, 2006; Lasaga and Luttge, 2001; Kurganskaya and Lüttge, 2013). In their "dissolution
511 stepwave model", Lasaga and Lüttge (2001) underlined that etch pits contribute to the total
512 dissolution rate not only by locally enhancing the dissolution of the surface, but also by the
513 generation of "stepwaves" emanating from the nucleated pits. These stepwaves would lead to
514 a global retreat of the crystal surface by dissolving the material layer by layer. In our case, the
515 correlation between the density of etch pits and the retreat rate could explain the difference in
516 terms of reactivity between the two F1 faces and, in the same time, strengthen the hypothesis
517 that pit nucleation is a major driver of oligoclase crystal dissolution.

An explanation for these discrepancies in terms of pit density may rely on the anisotropic distribution of dislocations in the oligoclase structure. In minerals, dislocations are characterized by their Burgers vectors, which represent the magnitude and direction of the distortion resulting from a dislocation in a crystal lattice. Dislocations oriented following the Burgers vectors with the shortest length are generally favored, due to energetics reasons. In the case of feldspars, dislocations following the [001] direction are particularly abundant (Tullis, 1983), which is in strong agreement with our observations: while screw dislocations with [001] Burgers vectors may outcrop at the (001) surface, they do not outcrop at the (010) surface, possibly accounting for the observed different pit density between these two faces.

Another interesting result is that the surface retreat of these two flat faces evolves linearly with time (Figure 3 & 7), whereas etch pits continuously nucleate on their surface, generating pit walls, which represent additional surface area exposed to the fluid. Moreover, considering that the (001) and (010) faces are among the least reactive faces of the crystal, the generated facets would be expected to be as/more reactive as/than the face on which the pits nucleate, according to the PBC theory. For all these reasons, one could expect an increase in dissolution rates of these 2 flat faces with time. Pollet-Villard et al. (2016b), who also measured constant dissolution rates for F faces of a K-feldspar, observed and demonstrated that the exposure to the solution of pit walls with a reactivity greater than that of the face on which they nucleate, was responsible for an initial increase of the dissolution rate, which eventually reaches a steady-state after a short transient period. As a consequence, the initial increase of the dissolution rate was out of reach of their measurements conducted on longer durations. A similar explanation may be proposed in the present study. This result contrasts with our observations for the S face, which offers much more initial reactive sites: in this case, the evolution of the topography of the surface has a clear impact on the dissolution rates after a few days of experiment.

4.3. Formation and impact of ASSLs

4.3.1 Formation of surface layers inferred from fluid and SEM data

Amorphous layers of variable thicknesses are generally found to cover the surface of altered silicate minerals/glasses. In the present study, the direct observation of such layers on crystalline samples reacted in Si-low solution was out of reach of the analytical techniques we used (SEM). In contrast, the formation of Si-rich layers was confirmed for all (crystalline and amorphous) samples reacted in Si-rich solutions at pH 1.5, as revealed by EDX analyses, where the Al/Si ratio of the surface of reacted samples was systematically lower than that of the pristine samples (see Supplementary Data).

Whereas no Si-rich layers were suspected to form on crystalline samples reacted at pH 10 (see section 3.2), the slight but systematic lack of Si released in the fluid for pH 1.5 experiments may be attributed to the formation of thin Si-rich layers, since the solutions were not supersaturated with respect to any secondary Si-bearing solid neither at high, nor at ambient temperature in these experiments. The calculated thickness of these layers ranges from ~0 to 200 nm after 30 days of experiments (Table 6), in good agreement with the results reported by Hellmann (1995) for albite under similar conditions.

Similarly, the formation of altered layers on glass surface was inferred from the fluid data at pH 1.5. However, because the aqueous Al/Na ratio was not stoichiometric, the ASSLs do not have the chemical composition of pure SiO_2(am). Consequently, it cannot be considered that the density of these ASSLs corresponds to that of SiO_2(am), and their thicknesses could not be calculated using Eq. (3).

4.3.2 Impact of ASSL on oligoclase dissolution rate

Recent studies underlined the potential effect of surface layers on the dissolution rates, but some divergences remain with respect to the formation mechanisms of these layers and the impact of surface layer formation on the dissolution rates of silicate minerals (Oelkers, 2001;

Hellmann et al., 2003; Daval et al., 2009a; Daval et al., 2009b; Daval et al., 2013; Saldi et al., 2013; Saldi et al., 2015; Maher et al., 2016; Wild et al., 2016) and glasses (Cailleteau et al., 2008; Geisler et al., 2010; Verney-Carron et al., 2011; Geisler et al., 2015; Gin et al., 2015; Hellmann et al., 2015; Collin et al., 2018a; Collin et al., 2018b; Gin et al., 2018). In particular, the part of the interfacial zone between the surface of the silicate and the fluid (internal or external interface) that controls the dissolution reaction has long been debated (Zhu et al., 2006). Two theories can be put forward: (a) the dissolution process is driven by the thermodynamic properties of a leached layer, defining the chemical affinity with respect to the ASSL *(external interface)* or (b) an ASSL is formed by an interfacial dissolution/precipitation process and, when the layer is not passivating, the fluid can access the pristine surface of the silicate *(internal interface)*, where the rate-limiting reactions may take place.

At pH 1.5, several lines of evidence suggest that the ASSL formed on the crystalline oligoclase are non-passivating:

(i) If the layers were passivating, one could have expected that the dissolution rate of a given face would correspond to the dissolution rate of the ASSL. The clear dissolution anisotropy rules out this assertion, suggesting that oligoclase dissolution is not controlled by a same unique surface layer. Therefore, the rate-limiting reactions are located at the internal ASSL/pristine solid interface, suggesting that aqueous species can access the pristine surface;

(ii) In spite of the stabilization of the ASSLs in Si-rich solutions (inferred from the absence of surface retreat measured by VSI in the corresponding experiments), oligoclase keeps dissolving, as evidenced by the linear release of Na for all faces (except the (001) face, for which the release is more parabolic). These results indicate that oligoclase dissolution proceeds with little to no transport limitation of the reactive species within the ASSL, suggesting that the surface layers are intrinsically porous. This result is consistent with those

obtained by Wild at al. (2016) on labradorite altered at 80 °C, where passivation was not observed for pH < 2.5. The switch of layers transport properties for a threshold pH value may explain why in natural settings -where pH ranges from mildly acidic to slightly basic- passivation may occur (Nugent et al., 1998; Daval et al., 2018).

At pH 10, no ASSL was formed on the crystalline oligoclase surface in silica-low solutions as revealed by (i) the clear observation of etch pits (as mentioned by Ruiz-Agudo et al. (2012), the nucleation and growth of etch pits require a stoichiometric release of all ions to the solution), (ii) the stoichiometric Na/Si release, in agreement with previous dissolution studies conducted on alkali feldspars in alkaline media (e.g., Hellmann et al., 1997; Pollet-Villard et al., 2016a), (iii) the absence of any secondary phases revealed by SEM analyses. Note that the slight lack of Al in solution was attributed to an experimental artifact resulting from Al precipitation after sampling and before ICP analyses, as verified from duplicate experiments which revealed that the release of Al was strictly stoichiometric (see Supplementary Data.). In contrast, ASSLs did develop in silica-rich solutions, as suggested by the absence of surface retreat measured by VSI. Similarly to the pH 1.5 experiments, such layers are non-passivating, as suggested by the release rate of Na, which is similar in silica-low and silica-rich solutions (see Table 5). The transport properties of these layers are therefore even better than those developed at pH 1.5 on oligoclase surface in silica-rich solutions.

To summarize, the formation and stabilization of ASSLs on crystalline oligoclase has little to no impact on the release rate of Al and Na, suggesting that such ASSLs do not prevent the solution to reach the pristine crystalline surface, whatever the pH. Because this result does not depend on the crystallographic orientation, we can further suggest that the transport properties of ASSLs are isotropic, in agreement with the results of Wild et al. (2016) for labradorite feldspar at pH 1.5 and 80 °C.

Finally, the fluid data clearly indicate that the chemical composition of ASSLs formed on the oligoclase glass differs from that formed on crystalline oligoclase. The linear release of the three cations in low-Si solution at pH 1.5 and 10, even though the dissolution is not congruent, clearly indicates that the alteration layers are not passivating.

Conversely, in Si-rich solutions, a progressive decrease of the dissolution rate is observed, suggesting that a dense and transport-limiting layer builds up. The difference in chemical composition of the surface layers may explain why those formed on the glass keep dissolving in Si-rich solutions (see VSI data listed in Table 4), as opposed to the ASSLs formed on crystalline oligoclase. This observation questions the existence of a mechanistic continuum between the dissolution of glass and crystal of identical chemical composition, resulting in the discussion detailed in the next section.

4.4. Impact of amorphous/crystalline structure

At pH 1.5, oligoclase glass dissolves at a rate similar to that of the fastest studied faces of the crystal (Figure 14a). This observation indicates that under acidic pH conditions, and for this particular composition, the absence of long-range order only weakly impacts the dissolution rate of the solid. Notwithstanding, the fluid data suggest that the ASSLs do not have the same chemical composition on oligoclase glass and crystal. This result is particularly intriguing: if one assumes that both solids dissolve following an interfacial dissolution-reprecipitation mechanism, then the chemical composition of the interfacial precipitate should be the same, as long as the chemical composition of the fluid and solid phases are the same in all experiments, and provided that the nature of the substrate does not favor the nucleation of one phase at the expense of another. As a consequence, one of the simplest explanations to untie this knot is to assume that oligoclase glass and crystalline oligoclase do not dissolve following the same interfacial dissolution-reprecipitation mechanism. While the data collected

643 above for crystalline oligoclase are consistent with an interfacial dissolution-reprecipitation
644 mechanism, ASSLs formed on the oligoclase glass may at least partly be formed by leaching.

645 To explore this idea, molecular dynamics simulations of crystal and glass structures
646 have been performed. Figure 15 shows that the structure of the glass is more open than that of
647 the crystal, with a small fraction of interstitials allowing water molecules to diffuse in (radius
648 > 1.3 Å). In the crystal, such voids do not exist. As a consequence, crystal dissolves only by
649 surface reactions, whereas glass may undergo both ion-exchange following water diffusion in
650 the solid, as well as surface reaction.

651 At pH 1.5, the linear release of sodium with time from glass may either be explained
652 by dissolution-reprecipitation (because this model assumes that the release of ions is not
653 transport-limited) or by preferential leaching, because the classical ion-exchange between
654 network modifiers and hydronium ions, which occurs following (Bunker, 1994):

655 $\equiv Si{-}O^{-}\ldots Na^{+} + H_3O^{+} \leftrightarrows \equiv Si{-}OH + Na^{+} + H_2O$

656 and results in a square root time-dependent release of Na (Doremus, 1979; Boksay, 1979) is
657 unlikely here, since sodium ions do not act as glass modifiers. Instead, the vast majority of
658 them charge compensate AlO_4^- units forming a strong ionic bond with O. Because of the
659 difference in the chemical bonding between Na^+ and H^+ with O, H^+ cannot charge compensate
660 AlO_4^- (Uchino et al., 1993). Therefore, it is not surprising that in our study — but also for
661 jadeite and nepheline glasses, which both have an Al/Na ratio of 1 — the Na release under
662 acidic pH conditions is not parabolic but linear and almost congruent with Al release
663 (Hamilton et al., 2001). As a consequence, under acidic conditions, oligoclase crystal and
664 oligoclase glass may dissolve following either the same or slightly different mechanisms due
665 to the more open glassy structure. This difference remains small because of the absence of
666 non-bridging oxygen (NBO) in the glass.

667 At pH 10, the oligoclase glass dissolves 10 to 20 times faster than its crystalline
668 equivalent (Table 5, Figure 14b). The altered layers formed on glass contain Si and Al,
669 whereas no surface layers were formed on the various crystal faces.

670 In order to explain the effect of pH on the behavior of the two solids, let us first
671 consider that the rate-limiting steps of aluminosilicate dissolution are pH-dependent. In acidic
672 conditions, hydrolysis of Si-O-Al dominates network dissolution (Xiao and Lasaga 1995),
673 whereas in basic conditions, either hydrolysis of deprotonated silanol groups or direct
674 nucleophilic attack of Si by OH^- are responsible for network dissolution. The density of
675 critical bonds (Si-O-Si in alkaline pH, Si-O-Al in acidic pH) is then a key factor controlling
676 matrix dissolution. At basic pH, the preferential attack of Si results in a majority of residual
677 Q_1^{Al} with no connectivity with the other Al. Then, two scenarios may be envisioned,
678 depending on the structure of the considered solid: regarding oligoclase crystal, the absence of
679 interstitials limits the reaction front at the mineral/water interface, and the removal of the
680 remaining Al is required for dissolution to go on. This is consistent with the step retreat
681 mechanism that was invoked to explain oligoclase dissolution anisotropy (which implies a
682 sequential, congruent removal of the atomic planes), and with the absence of surface layers in
683 the Si-low experiments. On the other hand, water percolation in the more open glassy
684 structure may result in surface layers that contain Al, as reported in the present study. As a
685 consequence, the oligoclase glass dissolves in basic pH as a SiO_2 polymorph does, i.e., much
686 faster than the crystal because of the structural disorder of the glass. These simple
687 considerations are in agreement with Hamilton et al (2001), who studied the dissolution of
688 albite (Al/Si: 1/3), jadeite (Al/Si: 1/2) and nepheline (Al/Si: 1/1) glasses between pH 1 and 12.
689 They showed that the higher the Al/Si ratio in the glass, the greater its dissolution rate in
690 acidic pH, whereas the rates are very close at pH 12, at least for albite and jadeite glasses.

691 To summarize, supposing that oligoclase glass and crystalline oligoclase do not
692 dissolve following the same mechanisms also helps explain the apparent contradiction
693 between the reactivity of the solids for the considered pH.
694
695 # 5. Conclusions
696 Investigating the dissolution of oligoclase glass and crystalline oligoclase under
697 identical chemical composition of the solutions enabled us to reach the following conclusions
698 regarding the impact of atomic ordering on silicate dissolution rates and mechanisms:
699 (i) The dissolution of crystalline oligoclase is anisotropic, and the face-specific
700 dissolution rate is in reasonable agreement with the periodic bond chain theory, both at acidic
701 and basic pHs.
702 (ii) Si-rich ASSLs developed on the surface of crystalline oligoclase at acidic pH are
703 non-passivating, and most likely formed by an interfacial dissolution-reprecipitation
704 mechanism.
705 (iii) The dissolution rate of oligoclase glass is similar to the fastest dissolving face at
706 acidic pH, and is more than an order of magnitude greater at basic pH.
707 (iv) The abovementioned discrepancy, coupled to the inferred difference of chemical
708 compositions of ASSLs between oligoclase crystal and oligoclase glass, and the results of
709 molecular dynamics support the idea that oligoclase glass may not dissolve according to the
710 exact same mechanisms as crystalline oligoclase, as oligoclase glass may undergo preferential
711 leaching of Al-Na moieties.
712 Taken together, these results question the existence of a mechanistic continuum
713 between the dissolution of silicate minerals and glasses, at least as basic pH. Further detailed
714 characterizations of the surface layers will help to unravel this assertion.
715

Acknowledgements:

The authors thank Gilles Morvan (LHyGeS), Rémy Saint-Lys (LHyGeS) and René Boutin (LHyGeS) for performing EBSD, providing supplementary data and helping with ICP-AES measurements, respectively. The author also thank the ECOS-MinCyT program for allowing the venue of Mélanie Vital in Strasbourg for several months. The authors are grateful to Thibault Charpentier (CEA Saclay) and Frédéric Angeli (CEA Marcoule) for the NMR analyses. The precious advices of Patrick Jollivet (CEA) were also particularly appreciated. Finally, the present paper benefited from the insightful comments and suggestions of Lawrence Anovitz (AE) and three reviewers including Jonathan Icenhower, which greatly improved an earlier version of the manuscript. This work was funded by Andra.

References

Arvidson RS and Lüttge A (2010) Mineral dissolution kinetics as a function of distance from equilibrium – New experimental results. *Chem. Geol* **269**, 79-88.

Bandstra JZ and Brantley SL (2008) Surface evolution of dissolving minerals investigated with a kinetic Ising model. *Geochim. Cosmochim. Acta* **72**, 2587-2600.

Bouyer F, Geneste G, Ispas S, Kob W and Ganster P (2010) Water solubility in calcium aluminosilicate glasses investigated by first principles techniques. *J. Solid State Chem.* **183**, 2786-2796.

Bunker BC (1994) Molecular mechanisms for corrosion of silica and silicate glasses. *Journal of Non-Crystalline Solids* **179**, 300-308.

Burch TE, Nagy KL, Lasaga AC (1993) Free energy dependence of albite dissolution kinetics at 80°C and pH 8.8. *Chem Geol* **105**, 137-162.

Cailleteau C, Angéli F, Devreux F, Gin S, Jestin J, Jollivet P and Spalla O (2008) Insight into silicate-glass corrosion mechanisms. *Nature Materials* **7**, 978-983.

Casey WH (2008) Glass and mineral corrosion dynamics and durability. *Nature Materials* **7**, 930-932.

Collin M, Fournier M, Frugier P, Charpentier T, Moskura M, Deng L, Ren M, Du J and Gin S (2018a) Structure of International Simple Glass and properties of passivating layer formed in circumneutral pH conditions. *Npj Materials Degradation* **2**, article n°4.

Collin M, Fournier M, Charpentier T, Moskura M and Gin S (2018b) Impact of alkali on the passivation of silicate glass. *Npj Materials Degradation* **2**, article n°16.

Daval, D, Calvaruso C, Guyot F, Turpault MP (2018) Time-dependent feldspar dissolution rates resulting from surface passivation: Experimental evidence and geochemical implications. *Earth Planet Sc Lett* **498**, 226-236.

Daval D, Martinez I, Corvisier J, Findling N, Goffe B and Guyot F (2009a) Carbonation of Ca-bearing silicates, the case of wollastonite: experimental investigations and kinetic modelling. *Chem. Geol.* **265**, 63-78.

Daval D, Martinez I, Guigner JM, Hellmann R, Corvisier J, Findling N, Dominici C, Goffe B and Guyot F (2009b) Mechanism of wollastonite carbonation deduced from micro- to nanometer length scale observations. *Am. Mineral.* **94**, 1707-1726.

Daval D, Hellmann R, Corvisier J, Tisserand D, Martinez I and Guyot F (2010) Dissolution kinetics of diopside as a function of solution saturation state: Macroscopic measurements and implications for modeling of geological storage of CO2. *Geochim. Cosmochim. Acta* **74**, 2615-2633.

761 Daval D, Sissman O, Menguy N, Saldi GD, Guyot F, Martinez I, Corvisier J, Garcia B,
762 Machouk I, Knauss KG and Hellmann R (2011) Influence of amorphous silica layer
763 formation on the dissolution rate of olivine at 90°C and elevated pCO_2. *Chem. Geol.* 284,
764 193-209.

765 Daval D, Hellmann R, Saldi GD, Wirth R and Knauss KG (2013) Linkin nm-scale
766 measurements of the anisotropy of silicate surface reactivity to macroscopic dissolution rate
767 laws: new insights based on diopside. *Geochim. Cosmochim. Acta* **107**, 121-134.

768 Deng L, Du J (2018) Effects of system size and cooling rate on the structure and properties of
769 sodium borosilicate glasses from molecular dynamics simulation. *J. Chem. Phys.* **148**,
770 024504.

771 Deng L., Jincheng D. (2016) Development of effective empirical potentials for molecular
772 dynamics simulations of the structures and properties of boroaluminosilicate glasses. *J. Non-*
773 *Cryst. Solids* **453**, 177-194.

774 Dove PM, Nizhou H, Wallace AF and de Yoreo JJ (2008) Kinetics of amorphous silica
775 dissolution and the paradox of the silica polymorphs. *Proc Natl Acad Sci USA* **105**, 9903-
776 9908.

777 Ducasse T., Gourgiotis A., Pringle ., Moynier F. and Gin S. (2018) Alteration of synthetic
778 basaltic glass in silica saturated conditions : Analogy with nuclear glass. *Appl. Geochem.* 97,
779 19-31.

780 Emmanuel S and Levenson Y (2015) Quantifying micron-scale grain detachment during
781 weathering experiments on limestone. *Geochim. Cosmochim. Acta* **173**, 86-96.

782 Fenter P, Zapol P, He H and Sturchio NC (2014) On the variation of dissolution rates at the
783 orthoclase (001) surface with pH and temperature. *Geochim. Cosmochim. Acta* **141**, 598-611.

784 Fischer C, Arvidson RS and Lüttge (2012) How predictable are dissolution rates of crystalline
785 material? *Geochim. Cosmochim. Acta* **98**, 177-185.

786 Fischer C, Kurganskaya I, Schäfer T and Lüttge A (2014) Variability of crystal surface
787 reactivity: What do we know? *Appl Geochem* **43**, 132-157.

788 Fischer C, Finkeldei S, Brandt F, Bosbach D and Luttge A (2015) Direct measurement of
789 surface dissolution rates in potential nuclear waste forms: The example of pyrochlore. *Appl.*
790 *Mater. Interfaces* **7**, 17857-17865.

791 Fischer A and Lüttge A (2017) Beyond the conventional understanding of water-rock
792 reactivity. *Earth Planet. Sci. Lett.* **457**, 100-105.

793 Fisk, MR, Crovisier, J.-L., Honnorez, J., 2013. Experimental abiotic alteration of igneous and
794 manufactured glasses. Cr Geosci 345, 176-184.

795 Fisk, M.R., Giovannoni, S.J., Thorseth, I.H., 1998. Alteration of Oceanic Volcanic Glass:
796 Textural Evidence of Microbial Activity. Science 281, 978-980.

Frugier P, Gin S, Minet Y, Chave T, Bonin B, Godon N, Lartigue JE, Jollivet P, Ayral A, de Windt L and Santarini G (2008). SON68 nuclear glass dissolution kinetics: Current state of knowledge and basis of the new GRAAL model. *J. Nucl. Mater.* **380**, 8-21.

Galeczka I, Wolff-Boenisch D, Oelkers EH and Gislason SR (2014) An experimental study of basaltic glass-H_2O-CO_2 interaction at 22 and 50°C: Implications for subsurface storage of CO_2. *Geochim. Cosmochim. Acta* **126**, 123-145.

Geisler T, Janssen A, Scheiter D, Stephan T, Berndt J, Putnis A (2010) Aqueous corrosion of borosilicate glass under acidic conditions: A new corrosion mechanism. *J. Non-Cryst. Solids* **356**, 1458-1465.

Geisler T, Nagel T, Kilburn MR, Janssen A, Icenhower JP, Fonseca ROC, Grange M, Nemchin AA (2015) The mechanism of borosilicate glass corrosion revisited. *Geochim. Cosmochim. Acta* **158**, 112-129.

Gin S, Jollivet P, Fournier M, Angéli F, Frugier P and Charpentier T (2015) Origin and consequences of silicate glass passivation by surface layers. *Nature communications* **6**, 1-8.

Gin S, Neill L, Fournier M, Frugier P, Ducasse T, Tribet M, Abdelouas A, Parruzot B, Neeway J and Wall N (2016) The controversial role of inter-diffusion in glass alteration. *Chem. Geol* **444**, 115-123.

Gin S, Collin M, Jollivet P, Fournier M, Minet Y, Dupuy L, Mahadevan T, Kerisit S and Du J (2018) Dynamics of self-reorganization explain passivation of silicate glasses. *Nature communications* **9**, 2169.

Godinho JRA, Piazolo S, Evin LZ (2012) Effect of surface orientation on dissolution rates and topography of CaF_2. *Geochim. Cosmochim. Acta* **86**, 392-403.

Godinho JRA, Piazolo S, Evans L (2014a) Simlation of surface dynamics during dissolution as a function of the surface orientation: Implications for non-constant dissolution rates. *Earth Planet. Sci. Lett.* **408**, 163-170.

Godinho JRA, Piazolo S, Balic-Zunic T (2014b) Importance of surface structure on dissolution of fluorite: implications for surface dynamics and dissolution rates. *Geochim. Cosmochim. Acta* **126**, 398-410.

Golubev SV and Pokrovsky OS (2006) Experimental study of the effect of organic ligands on diopside dissolution kinetics. *Chem. Geol* **235**, 377-389.

Grambow B and Müller R (2001) First-order dissolution rate law and the role of surface layers in glass performance assessment. *J. Nucl. Mater.* **298**, 112-124.

Grambow B (2006) Nuclear waste glasses; how durable? *Elements* **2**, 357-364.

Gruber C, Zhu C, Bastian Georg R, Zakon Y, and Ganor J (2014) Resolving the gap between laboratory and field rates of feldspar weathering. *Geochim. Cosmochim. Acta* **147**, 90-106.

832 Hamilton JP, Brantley SL, Pantano CG, Criscenti LJ and Kubicki JD (2001) Dissolution of
833 nepheline, jadeite and albite glasses: Toward better models for aluminosilicate dissolution.
834 Geochimica et Cosmochimica Acta 65, 3683-3702.

835 Hellmann R (1997) The albite-water system: Part IV. Diffusion modeling of leached and
836 hydrogen-enriched layers. *Geochim. Cosmochim. Acta* **61**, 1595-1611.

837 Hellmann R and Tisserand D (2006) Dissolution kinetics as a function of the Gibbs free
838 energy of reaction: an experimental study based on albite feldspar. *Geochim. Cosmochim.*
839 *Acta* **70**, 364-383.

840 Hellmann R, Daval D and Tisserand D (2010) The dependence of albite feldspar dissolution
841 kinetics on fluid saturation state at acid and basic pH: progress towards a universal relation.
842 *Comptes Rendus Géoscience* **342**, 676-684.

843 Hellmann R, Wirth R, Daval D, Barnes JP, Penisson JM, Tisserand D, Epicier T, Florin B and
844 Hervig RL (2012) Unifying natural and laboratory chemical weathering with interfacial
845 dissolution-reprecipitation: A study based on the nanometer-scale chemistry of fluid-silicate
846 interfaces. *Chemical Geology* **294-295**, 203-216.
847

848 Hellmann R, Cotte S, Cadel E, Malladi S, Karlsson LS, Lozano-Perez S, Cabié M and Seyeux
849 A (2015) Nanometer-scale evidence for interfacial dissolution reprecipitation control of
850 silicate glass corrosion. *Nature Materials 14*, 307-311.

851 Icenhower JP and Steefel CI (2015) Dissolution rate of borosilicate glass SON68: A method
852 of quantification based upon interferometry and implications for experimental and natural
853 weathering rates of glass. *Geochim. Cosmochim. Acta* **157**, 147-163.

854 Johnson NC, Thomas K, Maher K, Rosenbauer RJ, Bird D, Brown Fr GE (2014) Olivine
855 dissolution and carbonation under conditions relevant for in situ carbon storage. *Chemical*
856 *Geology* **373,** 93-105.

857 Kerrache A, Delaye JM (2014) Interstitial sites for He incorporation in nuclear glasses and
858 links to the structure: Results from numerical investigation. *Nucl. Instrum. Methods Phys.*
859 *Res. B* **326**,269−272.

860 Kurganskaya, I., Luttge, A., 2013. A comprehensive stochastic model of phyllosilicate
861 dissolution: Structure and kinematics of etch pits formed on muscovite basal face. *Geochim*
862 *Cosmochim Acta* **120**, 545-560.

863 Libourel G, Verney-Carron A, Morlok A, Gin S, Sterpenich J, Michelin A, Neff D, Dillmann
864 P (2011) The use of natural and archeological analogues for understanding the long-term
865 behavior of nuclear glasses. *Comptes Rendus Geoscience* **343**, 237-245.

Li J, Chou M, Yuan S and Burruss RC (2013) Observations on the crystallization of spodumene from aqueous solutions in a hydrothermal diamond-anvil cell. *Geofluids* **13**, 467-474.

Lüttge A, Arvidson RS, Fischer C (2013) A stochastic treatment of crystal dissolution kinetics. *Elements* **9**, 183-188.

Maher K, Johnson NC, Jackson A, Lammers LN, Torchinsky AB, Weaver KL, Bird DK and Brown Jr GE (2016) A spatially resolved surface kinetic model for forsterite dissolution. *Geochim. Cosmochim. Acta* **174**, 313-334.

Malavasi G., Menziani M.C., Pedone A., Segre U. (2006) Void size distribution in MD-modelled silica glass structures. *J. Non-Cryst. Solids* **252**, 285-296.

Maldonado P, Godinho JRA, Evins LZ, Oppeneer PM (2013) Ab initio prediction of surface stability of fluorite materials and experimental verification. *J. Phys. Chem.* **117**, 6639-6650.

Mansas C, Delaye JM, Charpentier T, Bruguier F, Bouty O, Penelon B, Arena H, Rebiscoul D (2017) Drivers of water transport in glass: Chemical or topological effect of the glass network? *J. Phys. Chem. C* **121** 16201-16215.

Morin GP, Vigier N, Verney-Carron A (2015) Enhanced dissolution of basaltic glass in brackish waters: Impact on biogeochemical cylces. *Earth Planet. Sci. Lett.* **417**, 1-8.

Nugent MA, Brantley SL, Pantano CG, Maurice PA (1998) The influence of natural mineral coatings on feldspar weathering. *Nature* **395**, 588-591.

Palandri JL, Kharaka YK (2004) A compilation of rate parameters of water-mineral interaction kinetics for application to geochemical modeling, in: U.S. *Geological Survey*, O.F.R. (Ed.), p. 70.

Parruzot B, Jollivet P, Rébiscoul D and Gin S (2015) Long-term alteration of basaltic glass: Mechanisms and rates. *Geochim. Cosmochim. Acta* **154**, 28-48.

Pauling L.(1947) Atomic radii and interatomic distances in metals. *J. Am. Chem. Soc.* **69**, 542−553.

Pedone A., Malavasi G., Menziani M. C., Cormack, A. N., Segre, U. (2006) A new self-consistent empirical interatomic potential model for oxides, silicates and silica-based glasses. *J. Phys. Chem.* B **110** 11780-11795.

Pierce EM, Rodriguez EA, Calligan LJ, Shaw WJ and McGrail BP (2008) An experimental study of the dissolution rates of simulated aluminoborosilicate waste glasses as a function of pH and temperature under dilute conditions. *Appl. Geochem.* **23**, 2559-2573.

Pollet-Villard M, Daval D, Ackerer P, Saldi GD, Wild B, Knauss KG, Fritz B (2016a) Does crystallographic anisotropy prevent the conventional treatment of aqueous mineral reactivity? A case study based on K-feldspar dissolution kinetics. *Geochim. Cosmochim.* Acta **190**, 294-308.

Pollet-Villard M, Daval D, Fritz B, Knauss KG, Schäfer, G, Ackerer, P (2016b) Influence of etch pit development on the surface area and dissolution kinetics of the orthoclase (001) surface. *Chem. Geol.* **447**, 79-92.

Rébiscoul D, van der Lee A, Rieutord F, Né F, Spalla O, El-Mansouri A, Frugier P, Ayral A and Gin S (2004) Morphological evolution of alteration layers formed during nuclear glass alteration: new evidence of a gel as a diffusive barrier. *Jour. Nucl. Mater.* **326**, 9-18.

Ruiz-Agudo E, King HE, Patino-Lopez LD, Putnis CV, Geisler T, Rodriguez-Navarro C and Putnis A (2016) Control of silicate weathering by interface-coupled dissolution-precipitation processes at the mineral-solution interface. *Geology* **44**, 567-570.

Robin, V., Wild, B., Daval, D., Pollet-Villard, M., Nonat, A., Nicoleau, L., 2018. Experimental study and numerical simulation of the dissolution anisotropy of tricalcium silicate. Chem Geol 497, 64-73.

Saldi GD, Daval D, Morvan G and Knauss KG (2013) The role of Fe and redox conditions in olivine carbonation rates: An experimental study of the rate limiting reactions at 90 and 150°C in open and closed systems. *Geochim. Cosmochim. Acta* **118**, 157-183.

Saldi GD, Daval D, Guo H, Guyot F, Bernard S, Le Guillou C, Davis JA and Knauss KG (2015) Mineralogical evolution of Fe-Si rich layers at the olivine-water interface during carbonation reactions. *Am. Mineral.* **100**, 2655-2669.

Sissmann O, Brunet F, Martinez I, Guyot F, Verlaguet A, Pinquier Y and Daval D (2014) Enhanced olivine carbonation within a basalt as compared to single-phase experiments: reevaluating the potential of CO2 mineral sequestration. *Environ. Sci. Technol* **48**, 5512-5519.

Smith ME, Knauss KG, Higgins SR (2013) Effects of crystal orientation on the dissolution of calcite by chemical and microscopic analysis. *Chemical Geology* **360**, 10-21.

Saldi GD, Voltolini M, Knauss KG (2017) Effects of surface orientation, fluid chemistry and mechanical polishing on the variability of dolomite dissolution rates. *Geochim. Cosmochim. Acta* **206**, 94-111.

Shannon RD, Prewitt CT (1969) Effective ionic radii in oxides and fluorides. *Acta Crystallogr., Sect. B: Struct. Crystallogr. Cryst. Chem*. **25**, 925-946.

Tilocca A. (2013) Cooling rate and size effects on the medium-range structure of multicomponent oxide glasses simulated by molecular dynamics. *J. Chem. Phys.* **139**, 114501.

Tole M.P., Lasaga A.C., Patano C., White W.B. (1986) The kinetics of dissolution of nepheline ($NaAlSiO_4$). *Geochim. Cosmochim. Acta* **50**, 379-392.

Tullis, J. (1983) Deformation of feldspars. In: *Feldspar Mineralogy. Reviews in Mineralogy* **2**, 297-323.

939 Verney-Carron A., Gin S, Libourel G (2008) A fractured roman glass block altered for 1800
940 years in seawater: Analogy with nuclear waste glass in a deep geological repository. *Geochim.*
941 *Cosmochim. Acta* **72**, 5372-5385.
942
943 Vienna JD, Ryan JV, Gin S and Inagaki Y (2013) Current understanding and remaining
944 challenges in modeling long-term degradation of borosilicate nuclear waste glasses. *Int. J.*
945 *App. Glass Sci.* **4**, 283-294.
946
947 White AF and Brantley SL (2003) The effect of time on the weathering of silicate minerals:
948 why do weathering rates differ in the laboratory and field? *Chemical Geology* **202**, 479-506.
949
950 Wild B, Daval D, Guyot F, Knauss KG, Pollet-Villard M and Imfeld G (2016) pH-dependant
951 control of feldspar dissolution rate by altered surface layers. *Chem Geol.* **442**, 148-159.
952
953 Wolff-Boenisch D, Gislason SR, Oelkers EH, Putnis CV (2004) The dissolution rates of
954 natural glasses as a function of their composition at pH 4 and 10.6 and temperatures from 25
955 to 74°C. *Geochim. Cosmochim. Acta* **68**, 4843-4858.
956
957 Xiao Y. and Lasaga A.C. (1995) Ab initio quantum mechanical studies of the kinetics and
958 mechanisms of silicate dissolution: $H^+(H_3O^+)$ catalysis. *Geochim. Cosmochim. Acta* **58**, 5379-
959 5400.
960
961 Yang W. H., Kirkpatrick J. and Henderson D. M. (1986) High-resolution 29 Si, 27 Al and 23
962 Na NMR spectroscopic study of Al-Si disordering in annealed albite and oligoclase. *American*
963 *Mineralogist* **71**, 712-726.
964

Table

Table 1: Experimental parameters used for albite dissolution in Si-low and Si-rich experiments. Columns 2 and 5 refer to the initial S/V ratio (m^{-1}), columns 3 and 6 refer to the initial pH of the solution and columns 4 and 7 refer to the total time duration (days) of the experiments.

pH 1.5

	Si-low experiments			Si-rich experiments		
	S/V	pH	Exp. time	S/V	pH	Exp. time
(001)	0.68	1.52	39	0.89	1.49	46
(010)	0.53	1.50	40	0.52	1.51	46
$(10\bar{1})$	0.67	1.49	42	0.47	1.50	45
$(1\bar{1}1)$	0.35	1.53	39	0.14	1.47	29
Glass	1.08	1.47	30	0.48	1.54	30

pH 10

	Si-low experiments			Si-rich experiments		
	S/V	pH	Exp. time	S/V	pH	Exp. time
(001)	0.65	10.22	30	0.88	10.10	30
(010)	0.51	10.15	30	0.66	10.05	30
$(10\bar{1})$	0.67	10.03	31	0.49	10.20	30
$(1\bar{1}1)$	0.21	9.90	28	0.28	10.16	30
Glass	1.15	10.11	30	0.88	10.07	30

Table 2: Force field adjustable parameters.

	A_{ij} (eV)	ρ_{ij} (Å)	C_{ij} (eV.Å^6)
Si-Si	834.40	0.29	0.0
Si-Al	646.67	0.12	0.0
Si-O	45296.72	0.161	46.1395
Al-Al	351.94	0.36	0.0
Al-Na	175.21	0.13	0.0
Al-O	28287.0	0.172	34.76
Na-O	120360.22	0.17	0.0
O-O	9027.03	0.265	85.0321

Table 3: Si, Al and Na millimolal concentrations (analytical error of 10%) measured with ICP-AES in liquid aliquots obtained by regular sampling (4-5 mL, the time of each sampling is given in days) at pH 1.5 and pH 10 of (001), (010), $(10\bar{1})$, $(1\bar{1}1)$ surfaces of the albite crystal and amorphous samples (b.d.l.: below detection limit).

		Time	Si	Al	Na	*Time*	Si	Al	Na
		pH 1.5				**pH 10**			
Si-low experiments	(001)	**0**	0.001	b.d.l.	b.d.l.	**0**	0.001	b.d.l.	b.d.l.
		10	0.034	0.014	0.013	**4**	0.007	0.002	0.002
		20	0.113	0.044	0.035	**9**	0.014	0.004	0.003
		31	0.210	0.081	0.061	**14**	0.027	0.007	0.007
		39	0.300	0.111	0.087	**19**	0.047	0.011	0.011
						24	0.071	0.018	0.018
						30	0.102	0.026	0.026
	(010)	**0**	0.001	b.d.l.	b.d.l.	**0**	0.000	b.d.l.	b.d.l.
		10	0.023	0.009	0.009	**4**	0.003	0.001	0.001
		20	0.048	0.018	0.015	**9**	0.005	0.001	0.001
		31	0.078	0.029	0.023	**14**	0.009	0.002	0.002
		38	0.100	0.036	0.030	**19**	0.012	0.003	0.003
						24	0.019	0.005	0.005
						30	0.025	0.007	0.006
	$(10\bar{1})$	**0**	0.001	b.d.l.	b.d.l.	**0**	0.001	b.d.l.	0.002
		10	0.044	0.019	0.014	**5**	0.018	0.005	0.005
		21	0.143	0.056	0.042	**11**	0.035	0.010	0.009
		29	0.214	0.083	0.062	**17**	0.054	0.015	0.014
		42	0.340	0.129	0.098	**22**	0.075	0.020	0.020
						26	0.094	0.026	0.025
						31	0.119	0.034	0.033
	$(1\bar{1}1)$	**0**	0.001	b.d.l.	b.d.l.	**0**	b.d.l.	b.d.l.	b.d.l.
		10	0.046	0.014	0.010	**5**	0.008	0.001	0.001
		20	0.094	0.036	0.023	**10**	0.016	0.003	0.003
		31	0.151	0.058	0.040	**15**	0.023	0.005	0.006
		39	0.188	0.077	0.052	**22**	0.029	0.007	0.007
						28	0.036	0.009	0.010
	Glass	**0**	b.d.l.	b.d.l.	b.d.l.	**0**	b.d.l.	b.d.l.	b.d.l.
		5	0.021	0.010	0.012	**5**	0.050	0.023	0.024
		10	0.060	0.025	0.026	**10**	0.140	0.059	0.052
		15	0.104	0.040	0.040	**15**	0.244	0.093	0.080
		21	0.166	0.069	0.064	**21**	0.390	0.145	0.128
		27	0.262	0.103	0.099	**27**	0.614	0.230	0.198
		30	0.350	0.140	0.128	**30**	0.732	0.262	0.242

Si-rich experiments

(001)	**0**	b.d.l.	b.d.l.	**0**	b.d.l.	b.d.l.
	11	0.006	0.007	**5**	b.d.l.	0.003
	20	0.013	0.013	**10**	b.d.l.	0.007
	33	0.026	0.019	**16**	b.d.l.	0.012
	40	0.030	0.023	**20**	b.d.l.	0.015
	46	0.033	0.022	**25**	b.d.l.	0.018
				30	b.d.l.	0.023
(010)	**0**	b.d.l.	b.d.l.	**0**	b.d.l.	b.d.l.
	11	0.006	0.006	**5**	b.d.l.	0.005
	20	0.018	0.010	**10**	0.001	0.007
	33	0.027	0.018	**16**	0.001	0.012
	40	0.029	0.022	**20**	0.001	0.013
	46	0.031	0.023	**25**	0.001	0.015
				30	0.001	0.018
$(10\bar{1})$	**0**	b.d.l.	b.d.l.	**0**	b.d.l.	b.d.l.
	11	0.004	0.004	**5**	b.d.l.	0.002
	19	0.011	0.007	**10**	b.d.l.	0.003
	32	0.023	0.013	**16**	b.d.l.	0.005
	40	0.030	0.018	**20**	b.d.l.	0.005
	45	0.030	0.019	**25**	b.d.l.	0.006
				30	0.001	0.007
$(1\bar{1}1)$	**0**	b.d.l.	b.d.l.	**0**	b.d.l.	b.d.l.
	5	0.005	0.005	**5**	0.000	0.001
	9	0.008	0.007	**10**	0.000	0.003
	14	0.014	0.012	**16**	b.d.l.	0.004
	19	0.020	0.017	**20**	b.d.l.	0.005
	23	0.025	0.021	**25**	b.d.l.	0.006
	29	0.033	0.027	**30**	0.001	0.007
	35	0.041	0.033			
Glass	**0**	b.d.l.	b.d.l.	**0**	b.d.l.	b.d.l.
	5	0.001	0.002	**5**	0.002	0.010
	10	0.003	0.003	**10**	0.003	0.029
	14	0.004	0.005	**15**	0.005	0.038
	18	0.006	0.007	**21**	0.006	0.049
	22	0.009	0.010	**27**	0.008	0.060
				30	0.008	0.072

Table 4: Calculated dissolution rates (mol/m^2/s) at the external interface based on surface retreat measurements carried out on crystalline and glass surfaces dissolving at 90°C and pH 1.5 and 10 in Si-low and Si-rich solutions. Note that dissolution rates of the $(1\bar{1}1)$ face are not reported because they evolve with time, such that providing a mean dissolution rate over the duration of the experiment would be misleading. Dashes indicate that no surface retreat could be measured.

		CRYSTAL			GLASS
		(001)	(010)	$(10\bar{1})$	
pH 1.5	**Si-low**	7.5×10^{-9}	2.3×10^{-9}	9.5×10^{-9}	9.2×10^{-9}
	Si-rich	-	-	-	2.7×10^{-9}
pH 10	**Si-low**	9.5×10^{-10}	3.1×10^{-10}	1.0×10^{-9}	5.6×10^{-8}
	Si-rich	-	-	-	2.1×10^{-8}

Table 5: Calculated dissolution rates (mol/m^2/s) at the internal interface based on Na concentration in all experimental conditions (90°C. pH 1.5 and 10. Si-low and Si-rich solutions). Note that dissolution rates of the $(1\bar{1}1)$ face are not reported because they evolve with time, such that providing a mean dissolution rate over the duration of the experiment would be misleading.

		CRYSTAL			GLASS
		(001)	(010)	$(10\bar{1})$	
pH 1.5	**Si-low**	$3.6\text{x}10^{-8}$	$1.6\text{x}10^{-8}$	$3.8\text{x}10^{-8}$	$2.7\text{x}10^{-8}$
	Si-rich	$9.0\text{x}10^{-9}$	$4.0\text{x}10^{-9}$	$7.7\text{x}10^{-9}$	$6.7\text{x}10^{-9}$
pH 10	**Si-low**	$8.6\text{x}10^{-9}$	$3.4\text{x}10^{-9}$	$7.7\text{x}10^{-9}$	$6.1\text{x}10^{-8}$
	Si-rich	$7.0\text{x}10^{-9}$	$8.6\text{x}10^{-9}$	$5.3\text{x}10^{-9}$	$2.4\text{x}10^{-8}$

Table 6: Estimated thickness of the ASSLs developed after 30 days on the oriented surfaces of the crystal at pH 1.5, 90°C. The thicknesses were calculated using Eq. (3).

Crystallographic orientation	Layer thickness (nm)
(001)	189
(010)	117
$(10\bar{1})$	201
$(1\bar{1}1)$	~ 0

Figure

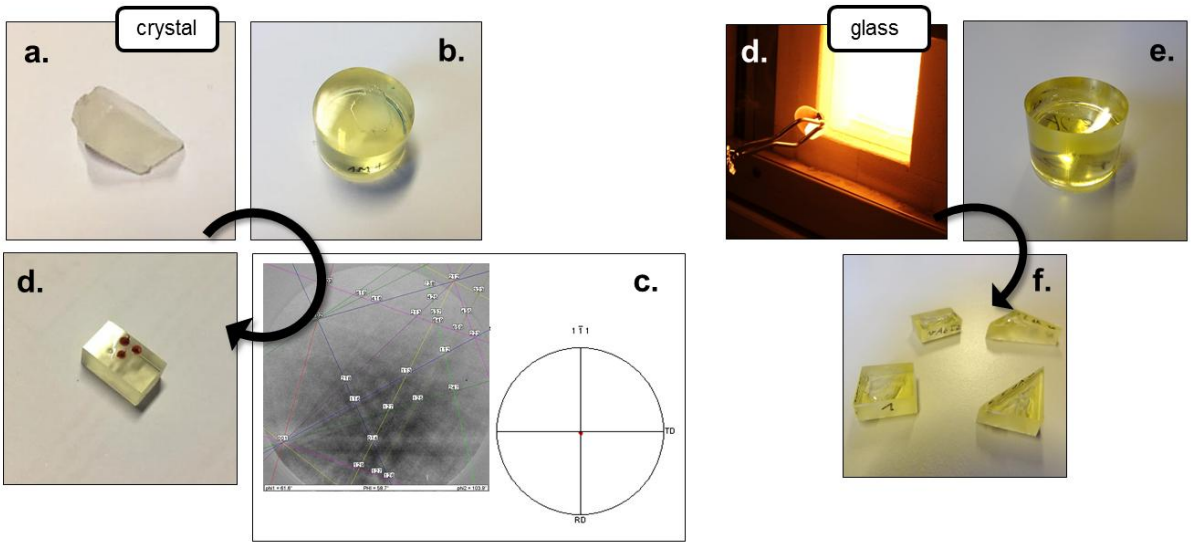

Figure 1: Crystal and glass sample preparations.

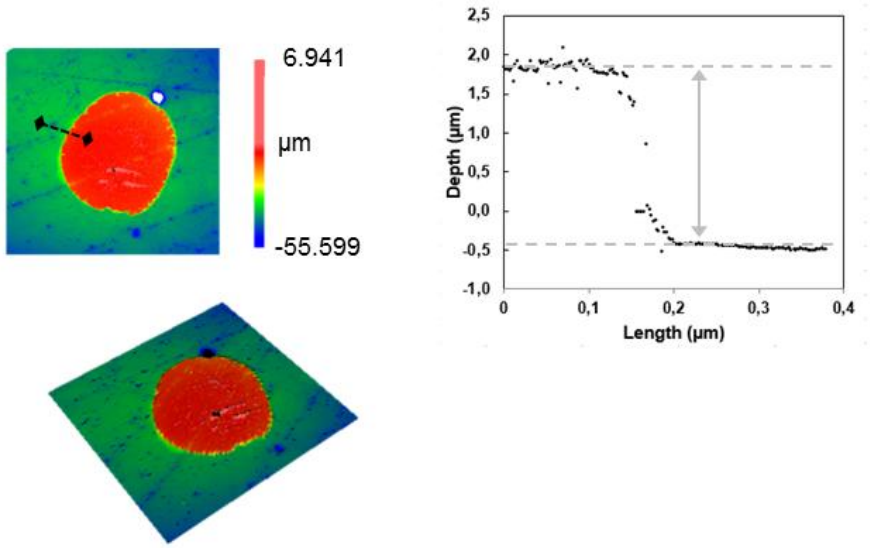

Figure 2: Surface retreat measurements with VSI. The masked surface is revealed by the presence of a raised flat area *(in red)* after the removal of the mask. This reference area contrasts with the dissolved surface *(in blue/green)* that has a height lower than the reference level.

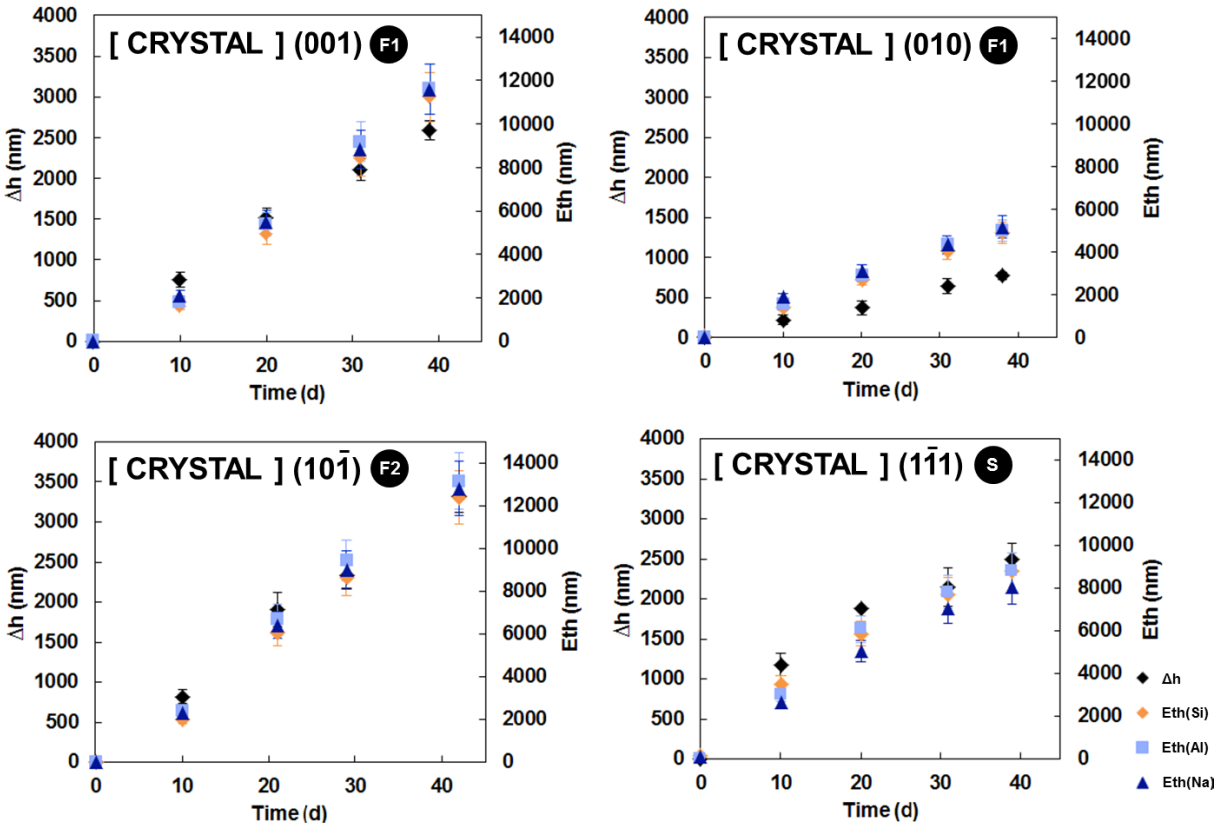

Figure 3: Surface retreat measurements (Δ*h, left vertical scale*) carried out by VSI during Si-low experiments at pH 1.5 and 90°C on (001), (010), (10$\bar{1}$), (1$\bar{1}$1) faces as a function of time and corresponding equivalent thickness (*Eth, right vertical scale*) calculated on the basis of Si, Al and Na release for the same dissolution experiments.

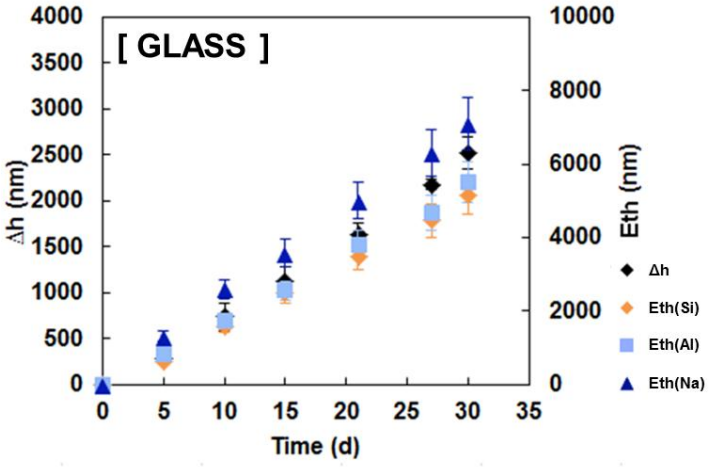

Figure 4: Surface retreat measurements (Δ*h, left vertical scale*) carried out using VSI during Si-low experiments at pH 1.5 and 90°C on glass surface as a function of time compared to equivalent thickness (*Eth, right vertical scale*) profiles calculated on the basis of Si, Al and Na release for the same dissolution experiment.

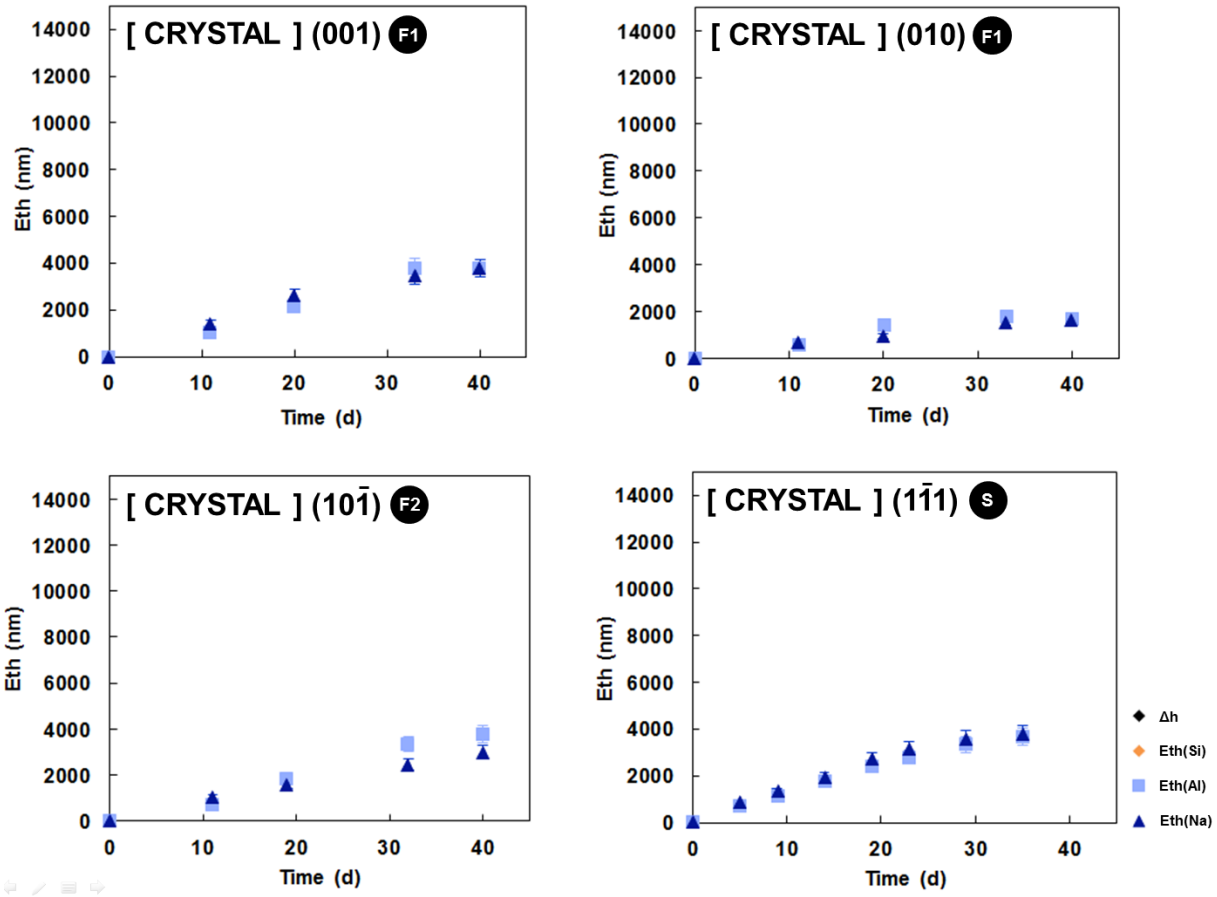

Figure 5: Equivalent thickness (*Eth*) profiles calculated on the basis of Al and Na release as a function of time during Si-rich experiments at pH 1.5 and 90°C.

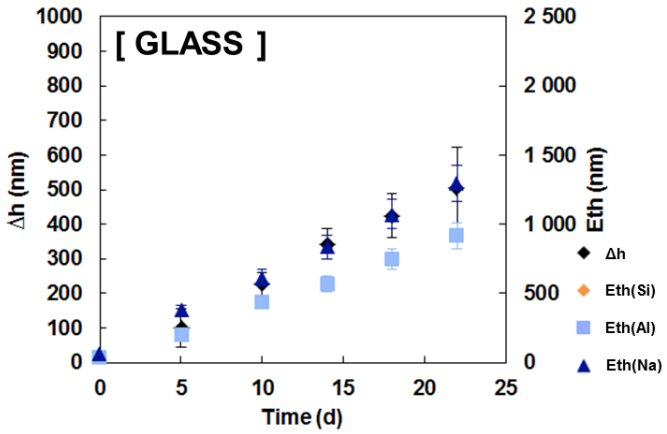

Figure 6: Surface retreat measurements (Δ*h, left vertical scale*) carried out using VSI during Si-rich experiments at pH 1.5 and 90°C on glass surface as a function of time compared to equivalent thickness (*Eth, right vertical scale*) profiles calculated on the basis of Al and Na release for the same dissolution experiment.

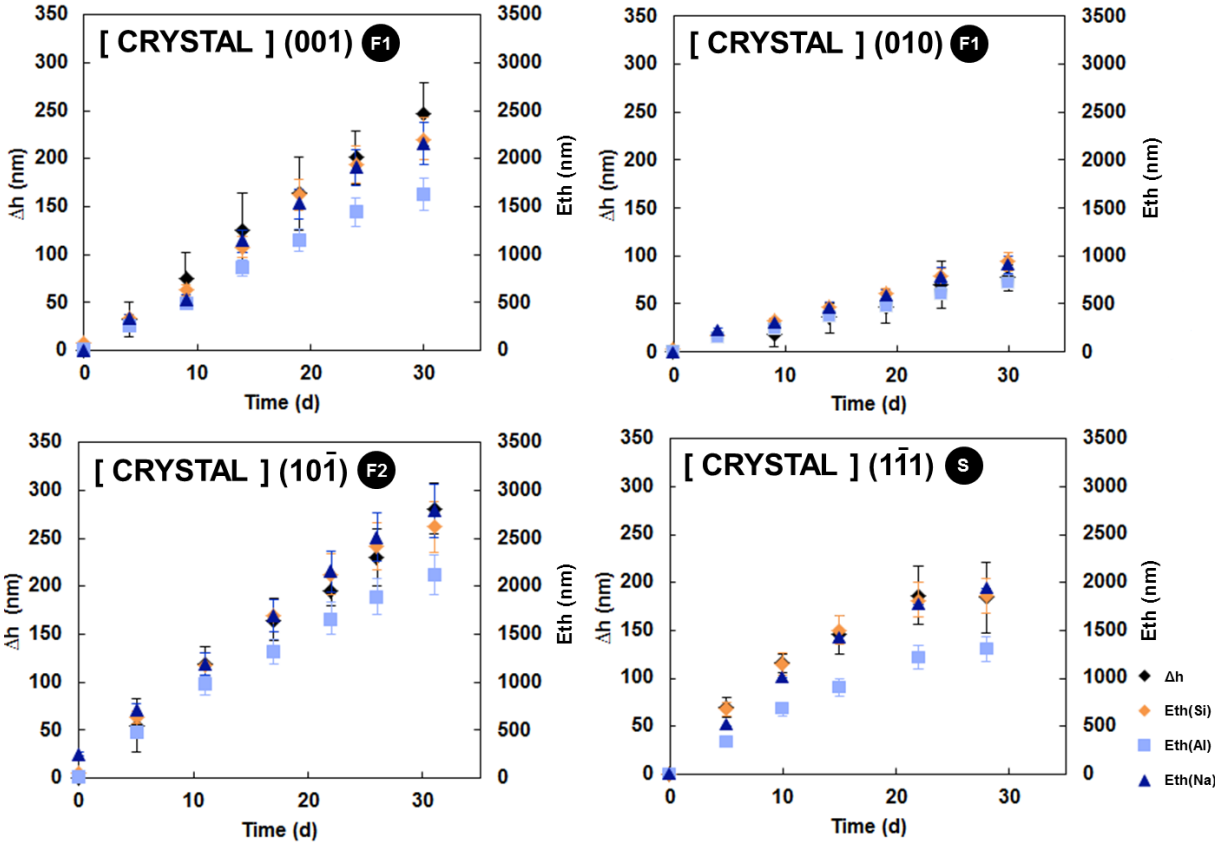

Figure 7: Surface retreat measurements (Δ*h*, *left vertical scale*) carried out by VSI during Si-low experiments at pH 10 and 90°C on (001), (010), (10$\bar{1}$), (1$\bar{1}$1) faces as a function of time compared to equivalent thickness (*Eth*, *right vertical scale*) profiles calculated on the basis of Si, Al and Na release for the same dissolution experiment.

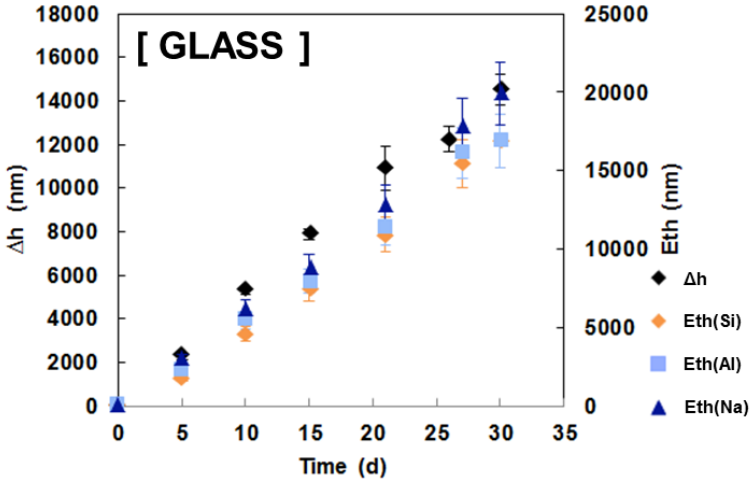

Figure 8: Surface retreat measurements (Δ*h*, *left vertical scale*) carried out by VSI during Si-low experiments at pH 10 and 90°C on glass surface as a function of time compared to equivalent thickness (*Eth*, *right vertical scale*) profiles calculated on the basis of Si, Al and Na release for the same dissolution experiment.

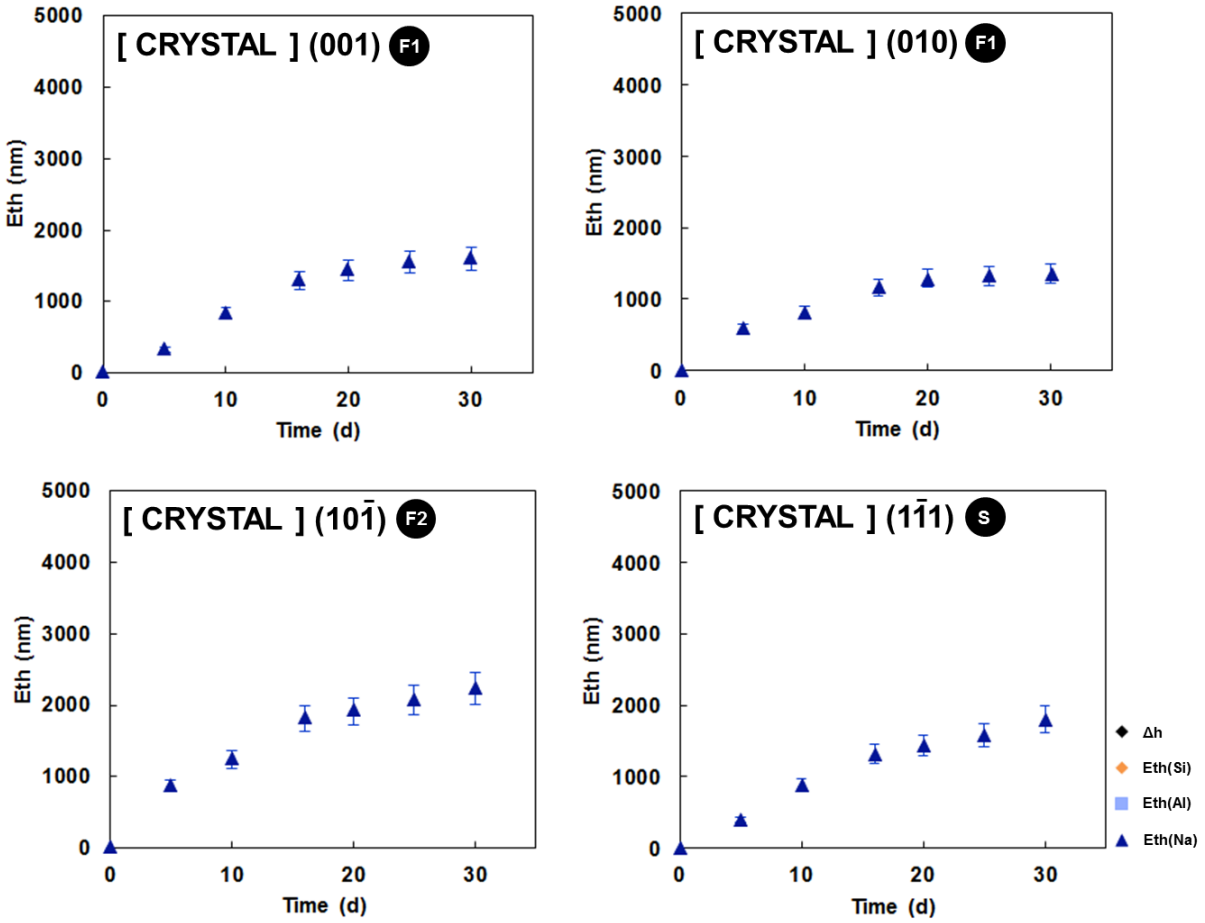

Figure 9: Equivalent thickness (*Eth*) profiles calculated on the basis of Na release as a function of time during Si-rich experiments at pH 10 and 90°C. Al data are not represented on the graphics as they are below detection limits.

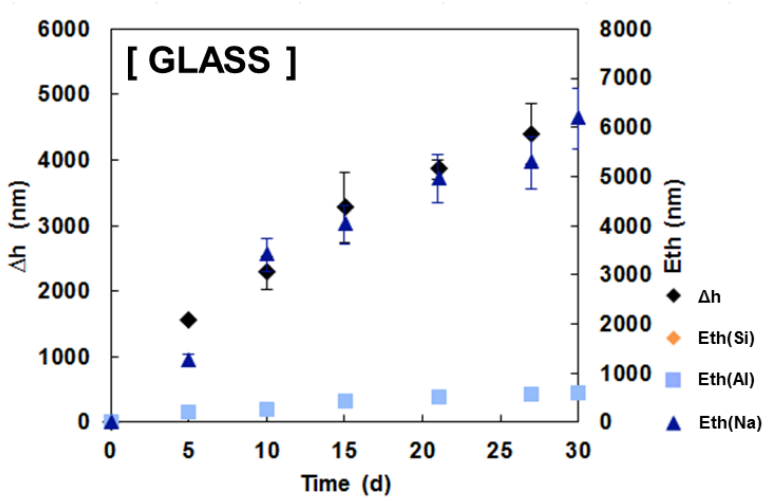

Figure 10: Surface retreat measurements (Δ*h*, *left vertical scale*) carried out by VSI during Si-rich experiments at pH 10 and 90°C on glass surface as a function of time compared to equivalent thickness (*Eth*, *right vertical scale*) profiles calculated on the basis of Al and Na release for the same dissolution experiment.

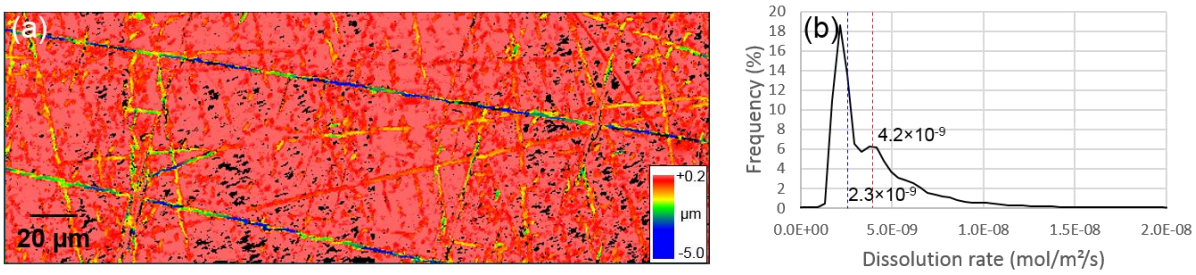

Figure 11: (a) VSI image of a subregion of the (010) surface located far from the masked area reacted at pH 1.5 in a silica-low solution (magnification: ×50). The image shows numerous polishing scratches where preferential dissolution occurred down to several microns below the mean elevation of the surface. (b) Corresponding rate spectrum calculated from (a). As can be seen, two specific modes can be evidenced, corresponding to the mean surface elevation and scratches, respectively. The dashed red line corresponds to the mean dissolution rate calculated based on the whole image (a). This value can be compared to the dissolution rate calculated in the immediate vicinity of the masked area, devoid of polishing scratches (dashed blue line).

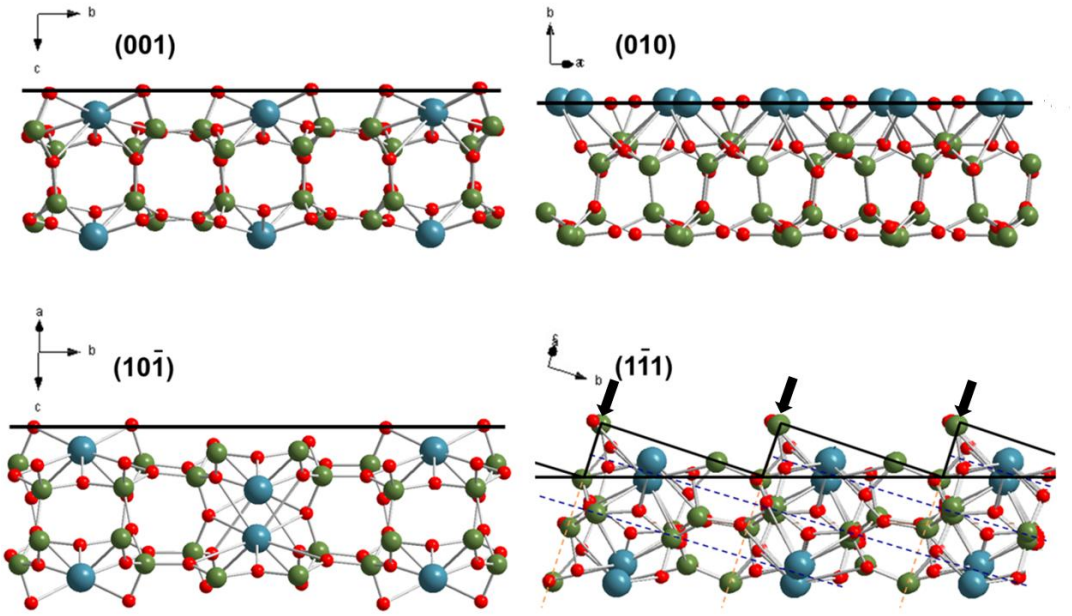

Figure 12: Representation of the cross section of the (001), (010), (10$\bar{1}$) flat faces and the (1$\bar{1}$1) stepped face of albite crystal (red, blue, and green balls represent O, Na, and Si/Al atoms, respectively). Steps of the (1$\bar{1}$1) are marked with an arrow, the intercepting planes forming the steps are marked with dashed lines. The planes are marked with continuous lines for faces (001), (010), (10$\bar{1}$). Images created with Diamond software.

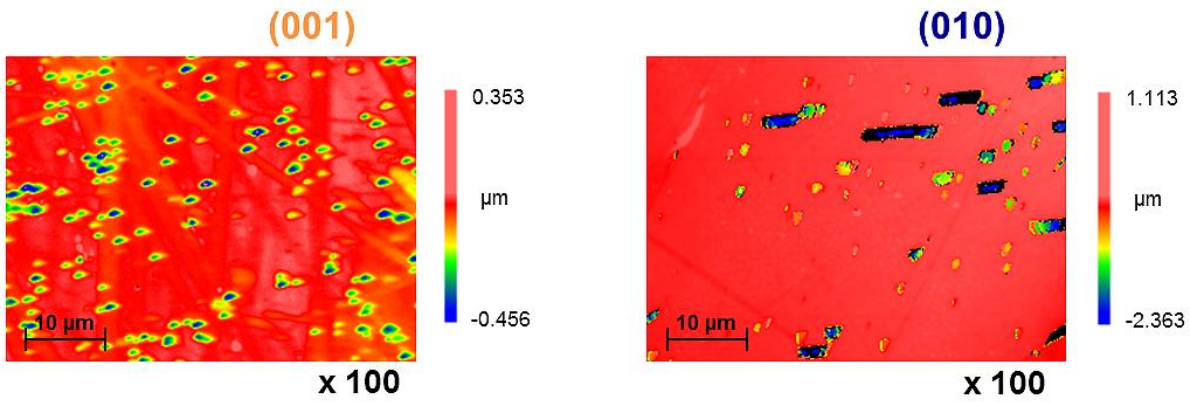

Figure 13: (001) and (010) albite surface topography after 30 days of experiments. VSI images processed with Metropro Software.

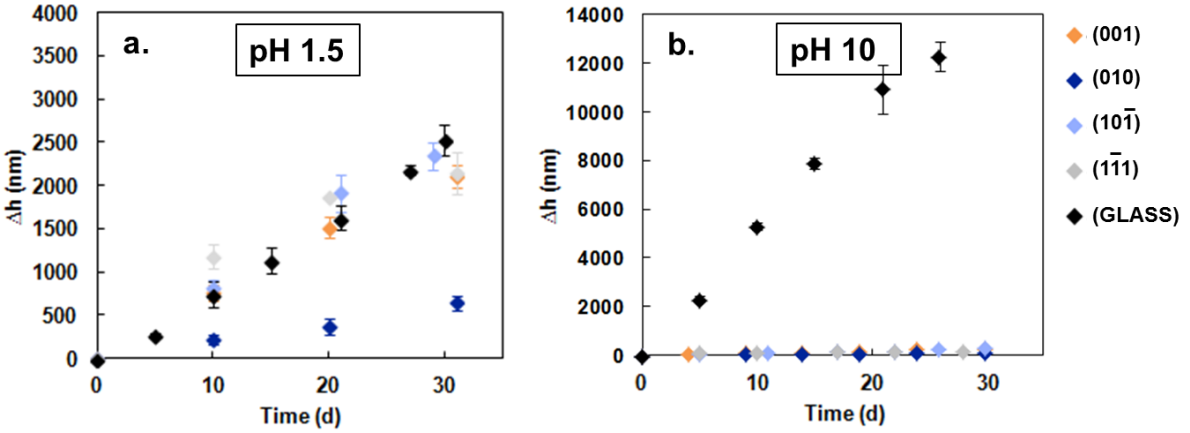

Figure 14: Surface retreats versus time for both crystalline (colored datapoints) and amorphous (black datapoints) samples measured in Si-low experiments at pH (a) 1.5 and (b) 10.

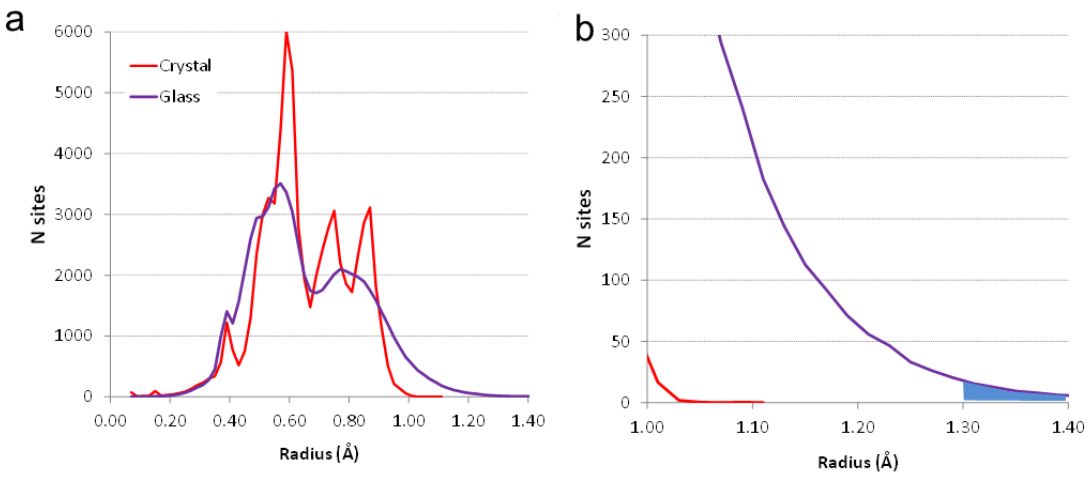

Figure 15: Molecular dynamics simulations of interstitials in albite crystal and glass structures. Figure a displays interstitial distribution for 10000 atoms (Figure a). Figure b displays interstitials distribution for radius greater than 1 Å. The blue area in figure b corresponds to interstitials large enough for water diffusion. Such interstices are not highlighted for the glass.